

1

2 **Strain signals governed by frictional-elastoplastic interaction of the upper plate and**
3 **shallow subduction megathrust interface over seismic cycles**

4 **Ehsan Kosari** ^{1,2†}, **Matthias Rosenau** ¹, **Onno Oncken** ^{1,2}

5 ¹Helmholtz Centre Potsdam, GFZ German Research Centre for Geosciences, Potsdam, Germany.

6 ²Department of Earth Sciences, Freie Universität Berlin, Berlin, Germany.

7

8 †Corresponding author: Ehsan Kosari (ehsan.kosari@gfz-potsdam.de)

9

10 **Key Points:**

- 11 • Analog earthquake cycle experiments provide observations to evaluate the surface strain
12 signals from the shallow megathrust.
- 13 • The extensional segment of the forearc overlays the seismogenic zone at depth.
- 14 • The strain state may remain quasi-stable over a few seismic cycles in the coastal zone.

15 **Abstract**

16 Understanding the behavior of the shallow portion of the subduction zone, which generates the
17 largest earthquakes and devastating tsunamis, is a vital step forward in the earthquake
18 geoscience. Monitoring only a fraction of a single megathrust earthquake cycle and the offshore
19 location of the source of these earthquakes are the foremost reasons for the insufficient
20 understanding. The frictional-elastoplastic interaction between the interface and its overlying
21 wedge causes variable surface strain signals such that the wedge strain patterns may reveal the
22 mechanical state of the interface. We employ Seismotectonic Scale Modeling and simplify
23 elastoplastic megathrust subduction, generate hundreds of analog seismic cycles at laboratory
24 scale, and monitor the surface strain signals over the model's forearc over high to low temporal
25 resolutions. We establish two coseismically compressional and extensional wedge configurations
26 to explore the mechanical and kinematic interaction between the shallow wedge and the
27 interface. Our results demonstrate that this interaction can partition the wedge into different
28 segments such that the anlastic extensional segment overlays the seismogenic zone at depth.
29 Moreover, the different segments of the wedge may switch their state from
30 compression/extension to extension/compression domains. We highlight that a more segmented
31 upper plate represents megathrust subduction that generates more characteristic and periodic
32 events. Additionally, the strain time series reveals that the strain state may remain quasi-stable
33 over a few seismic cycles in the coastal zone and then switch to the opposite mode. These
34 observations are crucial for evaluating earthquake-related morphotectonic markers (i.e., marine
35 terraces) and short-term interseismic GPS time-series onshore (coastal region).

36 **1 Introduction**

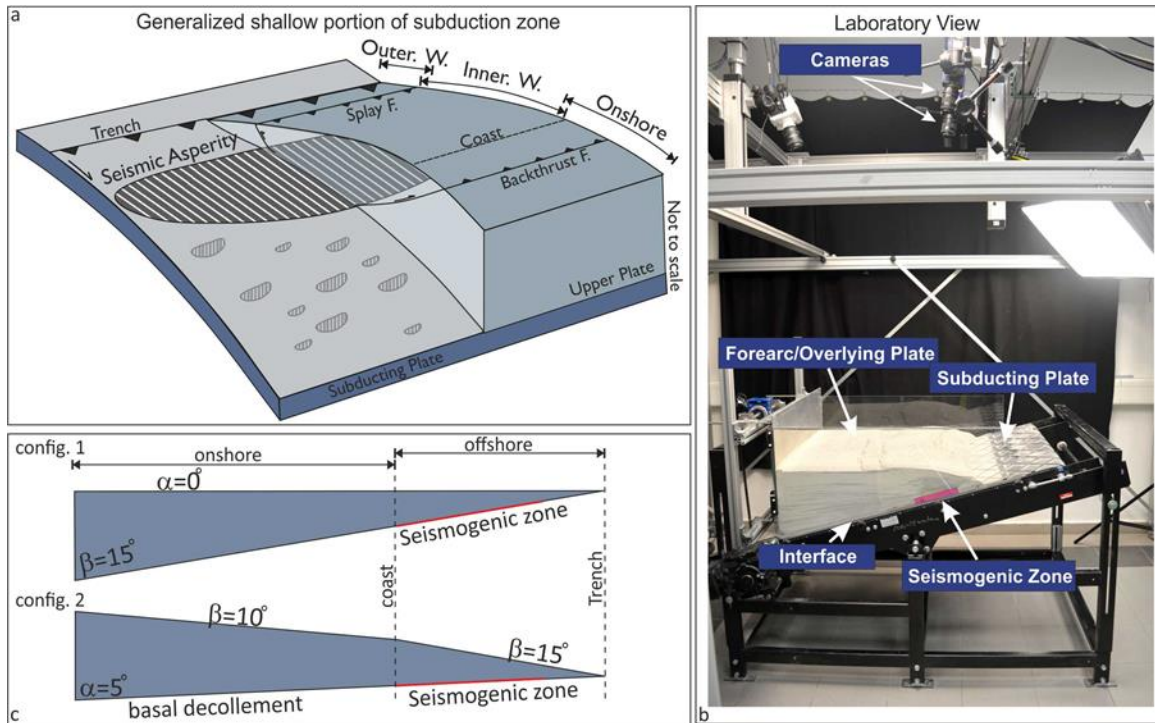
37 Estimating the interseismic coupling is the foremost approach to evaluate the earthquake
38 potential of subduction megathrusts (e.g., Chlieh et al., 2008; Moreno et al., 2010; Wallace et al.,
39 2012; McCaffrey et al., 2013; Métois et al., 2013; Schmalzle et al., 2014). While both up-dip and
40 down-dip limits of megathrust ruptures are typically located offshore and near the shore,
41 respectively, centuries-long recurrence intervals of the subduction megathrust earthquakes and
42 geodetically insufficiently instrumented seafloors prevent us from achieving sufficient details of
43 the shallow part of the megathrust (Kosari et al., 2020; Williamson & Newman, 2018). For
44 instance, a weakly coupled interface had been predicted in NE Japan based on the incomplete
45 interseismic geodetic measurements before the 2011 Tohoku-Oki megathrust event (e.g.,

46 Loveless & Meade, 2011). However, the slip models of the earthquake itself derived from rare
47 offshore geodetic data suggested a coseismic trench-breaching rupture (e.g., Ozawa et al., 2011;
48 Simons et al., 2011; Sun, Wang, Fujiwara, Kodaira, & He, 2017). Besides short-term (geodetic)
49 elastic surface deformation information, it is considered worthwhile to explore long-term
50 (geologic) permanent deformation signals for potential diagnostic patterns linked to megathrust
51 behavior (Geersen et al., 2018; Jara-Muñoz et al., 2015; Madella & Ehlers, 2021; Malatesta et
52 al., 2021; Melnick et al., 2018; Molina et al., 2021; Normand et al., 2019; Ott et al., 2019;
53 Saillard et al., 2017). Hence, for the sake of completeness of seismotectonic insights, long-term
54 geological information should be referred to.

55 Elastoplastic deformation is the dominant process in the shallow portion of the subduction zones
56 (Wang & Hu, 2006), and the mechanical properties of the wedge and megathrust govern the
57 strain pattern in the upper plate. The strain signals could be accumulated over a single or many
58 seismic cycles and preserved as morphotectonic features (i.e., extensional, compressional, and
59 shear markers) (Baker et al., 2013; Delano et al., 2017; Loveless et al., 2009; Loveless et al.,
60 2010; Rosenau & Oncken, 2009), representing the mechanical state of the forearc (Cubas et al.,
61 2013a and 2013b). In an earthquake cycle, the mechanical state might be highly variable in the
62 upper plate (Kopp, 2013; Melnick et al., 2009). In other words, the rate-strengthening and rate-
63 weakening portions of the megathrust cause time and space variable strain fields and rates over
64 the forearc during a seismic cycle. For instance, the coastal region can typically be under
65 compression during the interseismic period and under extension during and immediately
66 following the coseismic stage. Understanding how this leads to coastal topography and offshore
67 bathymetry as a persistent marker over many seismic cycles is vital. Eventually, this may lead to
68 incremental upper plate evolution towards its critical geometry and shape the forearc
69 morphology (Cubas et al., 2013a and 2016; Wang & Hu, 2006).

70 It is not fully transparent that to what extent we may infer the seismic potential of the shallow
71 (offshore) portion of the megathrust via onshore observations. Furthermore, the potential
72 temporal linkage between strain states (elastic and plastic) at the positions of the coast, inner-,
73 and outer-wedge is not resolved. Finally, could permanent surface deformation (i.e., plastic
74 strain) be reliably used as a clue for inferring the zones with megathrust earthquake potential? In
75 an attempt to answer these questions, we employ Seismotectonic Scale Modeling (Rosenau et al.,
76 2017 and 2009) to generate physically self-consistent analog megathrust earthquake ruptures and

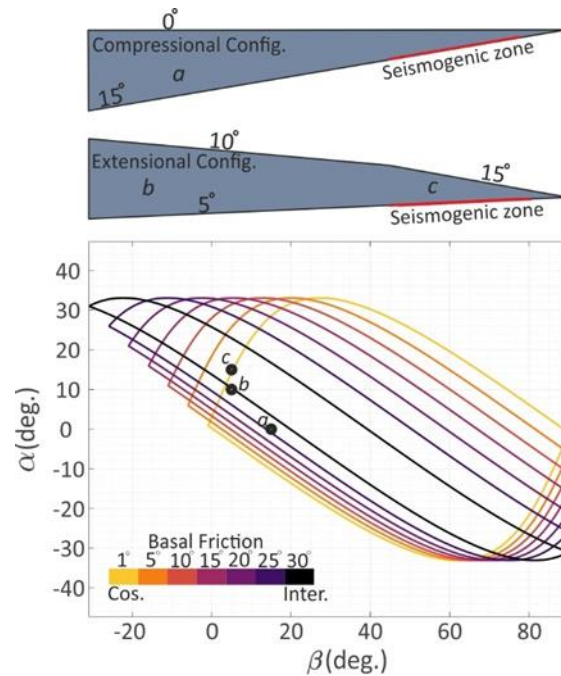
77 seismic cycles at the laboratory scale (Figure 1).



78
79
80 Figure 1: a: Generalized shallow portion of the subduction zone. The structures in the upper plate and
81 subducting plate are simplified. This schematic has been considered as a base for our analog
82 seismotectonic model. b: Laboratory view of our experiment. The main part of the analog model is
83 labeled in the image. c: 2d view of the two evaluated configurations in this study. The projection of the
84 down-dip limit of the stick-slip materials is defined as the coastal area. Alpha (α) and beta (β) represent
85 the surface and basal decollement, respectively.

86 This method has been used to study the interplay between short-term elastic (seismic) and long-
87 term permanent deformation (Rosenau and Oncken 2009). For mimicking the megathrust seismic
88 cycle and its associated surface deformation, we use a zone of velocity weakening (stick-slip)
89 and an elastoplastic wedge while the wedge is continuously compressed via a basal conveyor belt
90 (Kosari et al., 2020; Rosenau et al., 2019). A stereoscopic image correlation technique has been
91 used to monitor the surface deformation of the analog model (Adam et al., 2005). Generating
92 hundreds of seismic cycles and monitoring the associated surface deformation allows us to
93 unwrap the surface signals related to frictional properties at depth (velocity weakening versus
94 velocity strengthening).

95



96
 97 Figure 2: Mechanical states of a wedge introduced by the critical taper theory for coseismically
 98 compressional and extensional experiments. The areas within the envelopes characterize stable regimes.
 99 The areas above and below the envelopes indicate unstable extensional and compressional regimes,
 100 respectively. The positions on the envelopes represent critically stable domains.

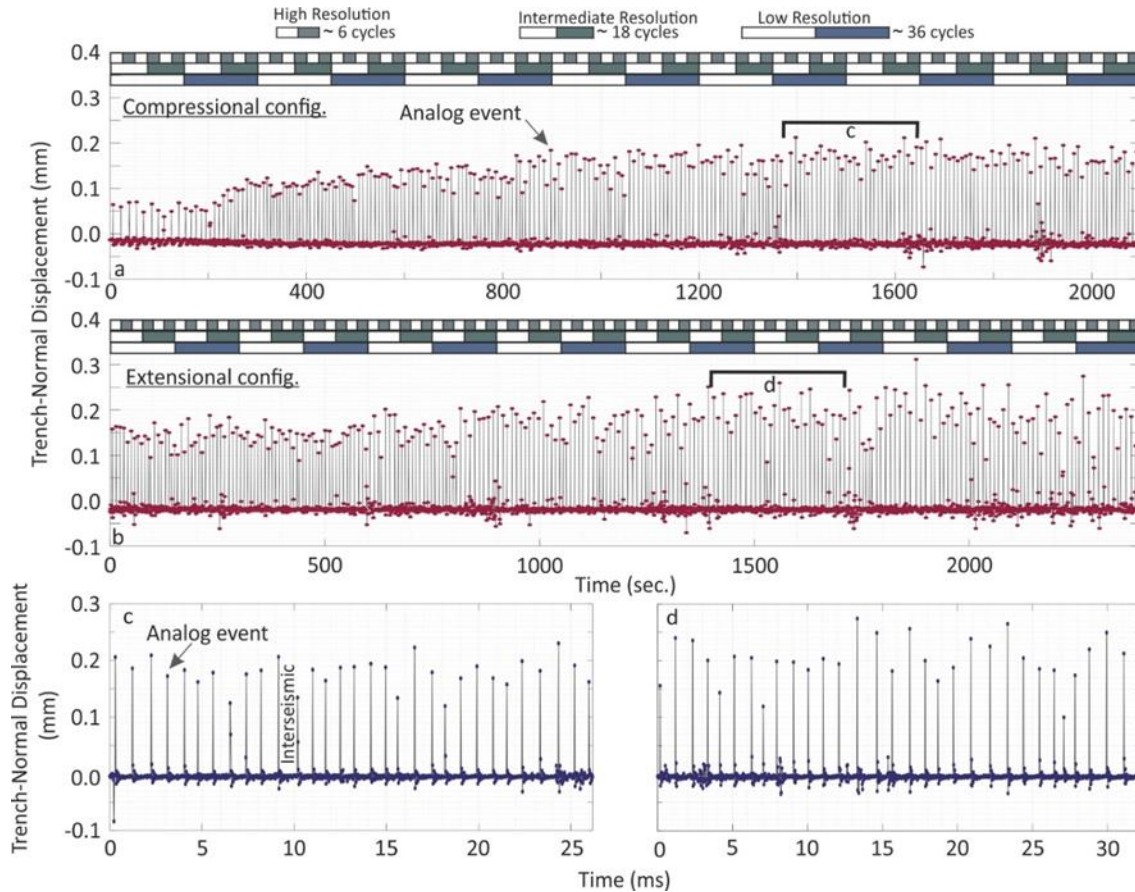
101

102 2 Seismotectonic Scale Modeling and Monitoring Techniques

103

104 Seismotectonic scale modeling is a unique technique to forward model the tectonic evolution
 105 over seismic cycles (e.g., Rosenau et al., 2017, and references therein). The approach has been
 106 used to study the interplay between short-term elastic (seismic) and long-term permanent
 107 deformation (Rosenau & Oncken, 2009), earthquake recurrence behavior and predictability
 108 (Corbi et al., 2020; 2019; 2017; Rosenau et al., 2019), the linkage between offshore geodetic
 109 coverage and coseismic slip models (Kosari et al., 2020) and details of the seismic cycle
 110 (Caniven & Dominguez, 2021). Analog models are downscaled from nature for the dimensions
 111 of mass, length, and time to maintain geometric, kinematic, and dynamic similarity by applying a
 112 set of dimensionless numbers (King Hubbert, 1937; Rosenau et al., 2009; 2017). The models
 113 generate a sequence of tens to hundreds of analog megathrust earthquake cycles, allowing the
 114 analysis of the corresponding surface displacement from dynamic coseismic to quasi-static
 115 interseismic stages.

116

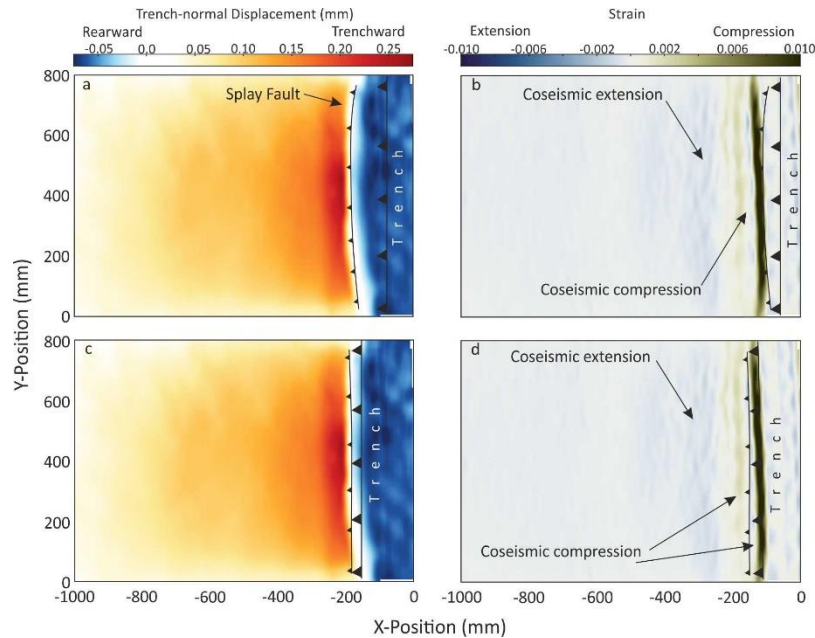


117

118 Figure 3: Analog earthquake catalog derived from surface displacement above the stick-slip zone on the
 119 model surface. The displacements larger than 0.05 millimeters represent an analog megathrust event
 120 ($M_w \geq 8$ at nature scale). Distance between two analog events represents the interseismic period in our
 121 experiments. a and b: all the events that occurred over model evolution from compressional and
 122 extensional experiments, respectively. Temporal processing windows for three different resolutions are
 123 differentiated by scale bars (see figures 7 and 8 for more details).c and d: a selected set of 30-32 analog
 124 megathrust events for evaluating surface displacement over the seismic cycles from both configurations,
 125 respectively.

126 In the 3-D experimental setup introduced in Kosari et al. (2020), a subduction forearc model is
 127 set up in a glass-sided box (1,000 mm across strike, 800 mm along strike, and 300 mm deep) on
 128 top of an elastic basal rubber conveyor belt (the model slab), and a rigid backwall. A wedge
 129 made of an elastoplastic sand-rubber mixture (50 vol.% quartz sand G12: 50 vol.% EPDM-
 130 rubber) is sieved into the setup representing a 240 km long forearc segment from the trench to
 131 the volcanic arc position (Figure 1).

132



133
 134 Figure 4: Surface horizontal displacement (a and c) and strain (b and d) maps derived from the
 135 extensional configuration. The upper panel represents the case of a megathrust event in which slip
 136 propagates on the splay faults (non-trench-reaching). The lower panel represents a megathrust event in
 137 which the slip reaches the trench (trench-reaching slip). The compressional (outer-wedge) and extensional
 138 (inner-wedge) segments.

139 At the base of the wedge, zones of velocity weakening controlling stick-slip (“seismic” behavior)
 140 are realized by emplacing compartments of “sticky” rice (“seismogenic zone”), which generate
 141 quasi-periodic slip instabilities while sheared continuously (Figure 1), mimicking megathrust
 142 earthquakes of different sizes and frequency (Figure 3). Large stick-slip instabilities are assumed
 143 to represent almost complete stress drops and recur at low frequency (~ 0.2 Hz) at a prescribed
 144 constant convergence rate of $50 \mu\text{m/s}$. This stick-slip behavior is intended to mimic rare great
 145 (M8-9) earthquakes with century-long recurrence intervals. The wedge itself and the conveyor
 146 belt respond elastically to these basal slip events similar to crustal rebound during natural
 147 subduction megathrust earthquakes. Upper plate faults (in our case, an “inland” backthrust fault
 148 and “offshore” forethrust and backthrust faults) emerge self-consistently downdip and up-dip of
 149 the seismogenic zone over multiple seismic cycles, as the effect of transient compression as
 150 documented in earlier papers (Kosari et al., 2020; Rosenau et al., 2009, 2010; Rosenau &
 151 Oncken, 2009).

152 Two different wedge geometries have been realized: a compressional configuration represents a
 153 transiently compressional wedge, and an extensional configuration, which is transiently

154 extensional according to Coulomb wedge theory (Figure 2). In the first configuration, hereafter
155 named “compressional configuration”, a flat-top ($\alpha=0$) elastoplastic wedge overlies a single large
156 rectangular in map view stick-slip patch (Width*Length=200*800 mm) over a 15-degree dipping
157 conveyor belt. In the second configuration, hereafter named “extensional configuration”, the
158 surface angle of the elastoplastic wedge varies from onshore ($\alpha=10$) to offshore ($\alpha=15$) segments
159 over a 5-degree basal decollement. The stick-slip zone in both configurations represents a system
160 of a homogeneous seismogenic zone with a temperature-controlled depth range and no variation
161 along strike generating M9 type megathrust events (Figure 1). According to Coulomb wedge
162 theory (Dahlen et al., 1984), the shallow wedge part of the compressional configuration
163 overlying the seismogenic zone is compressional in the interseismic stage when the basal friction
164 angle in the seismogenic zone is high (about 30°) and stable during the coseismic stage when the
165 basal friction in the seismogenic zone drops to zero. The coastal part of the wedge in the
166 compressional configuration is compressional throughout the seismic cycle as the basal friction
167 is high and rate-independent here. The extensional configuration, in contrast, has a coastal wedge
168 that is stable throughout the seismic cycle, whereas the shallow wedge overlying the seismogenic
169 zone is stable interseismically but becomes extensional during the coseismic stage. Both models
170 produce trench-reaching and non-trench-reaching slip analog megathrust events and push their
171 overlying wedges to compressional and extensional strain states (Figure 4).

172 To capture horizontal micrometer-scale surface displacements associated with analog
173 earthquakes and interseismic intervals at microsecond scale periods, a stereoscopic set of two
174 CCD (charge-coupled device) cameras (LaVision Imager pro X 11MPx, 14 bit) images the
175 wedge surface continuously at 4 Hz. To derive observational data similar to those from geodetic
176 techniques, that is, velocities (or incremental displacements) at locations on the model surface,
177 we use digital image correlation (DIC) (Adam et al., 2005) via the DAVIS 10 software
178 (LaVision GmbH, Göttingen/DE) and derive the 3-D incremental surface displacements at high
179 resolution (<0.1 mm) (Figure 3).

180 To calculate strain, we use the infinitesimal strain tensor because the condition of small strain is
181 met when resolving strains across the forearc during the interseismic period:

182

183

184

185

$$\begin{pmatrix} \varepsilon_{xx} & \varepsilon_{xy} & \varepsilon_{xz} \\ \varepsilon_{yx} & \varepsilon_{yy} & \varepsilon_{yz} \\ \varepsilon_{zx} & \varepsilon_{zy} & \varepsilon_{zz} \end{pmatrix}$$

186 where ε_{xx} represent the partial derivation of the trench-normal surface velocity component $\frac{\partial V_x}{\partial x}$
 187 showing trench-normal shortening: positive and negative values respectively represent
 188 compression and extension.

189

190 **3 Results and Interpretations**

191

192 The models' observations are presented in succession from long-term to short-term. First, we
 193 show how the upper plate structures evolve in a sequence over hundreds of analog earthquake
 194 cycles. We evaluate the spatial correlation between upper plate strain and topography evolution
 195 concerning locking and slip at the interface. Afterward, we spatially and temporally zoom in on a
 196 subset of seismic cycles to explore how strain states vary in different segments of the upper plate
 197 across seismic cycles. Eventually, the strain cycles in different wedge segments (i.e., outer-
 198 wedge, inner-wedge, and coast) are compared to check how similar they respond to the
 199 earthquake cycles in a homogeneous wedge with internal discontinuities (i.e., upper plate faults).

200

201 **3.1 Model Evolution from long to short timescales**

202 **3.1.1 Wedge anatomy: Final geometry, surface strain distribution, and structures formed**

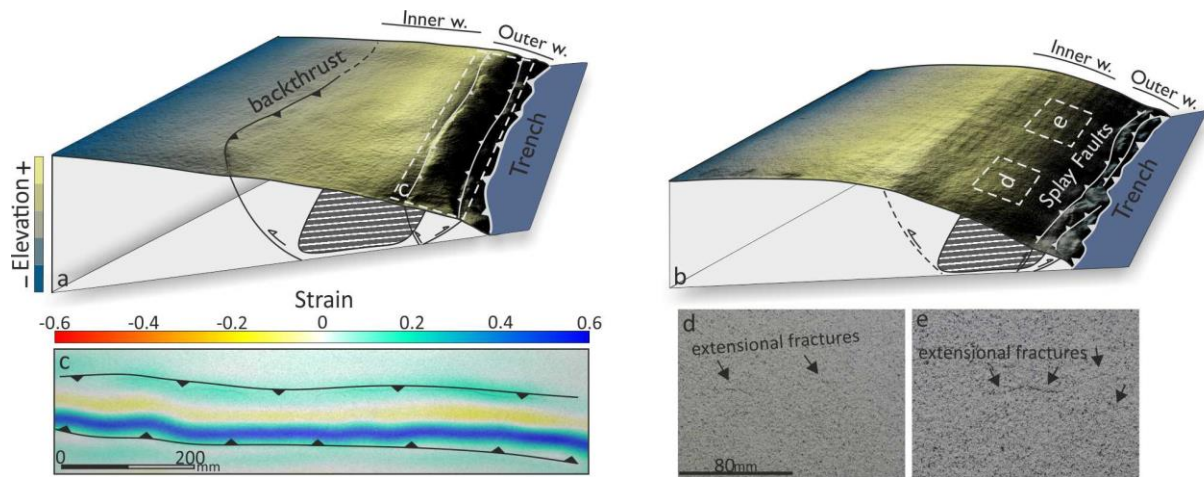
203

204 The cumulative strain pattern maps illustrate the long-term (hundreds of analog earthquake
 205 cycle) strain distribution in the upper plate (Figure 6). In the compressional configuration, three
 206 different wedge segments are observed: a compressional domain in the outer-wedge, an
 207 extensional domain in the inner-wedge, and a compressional domain in the coast. The outer-
 208 wedge compressional segment overlies the shallow creeping portion of the interface. Further
 209 rearward, the compression domain grades into an extensional domain in the inner-wedge
 210 overlying the velocity-weakening zone on the interface at depth. In our experiments, two main
 211 mechanisms could cause the permanent extensional strain in the inner-wedge: A minor anelastic
 212 component of the mainly elastic coseismic extension and the activity of splay fault-related folds.
 213 A compressional segment has also been observed in the coastal area, which may appear on the
 214 model's surface as a backthrust fault rooting in the frictional transition zone at the down-dip

215 limit of the velocity weakening zone (Figures 6).

216

217



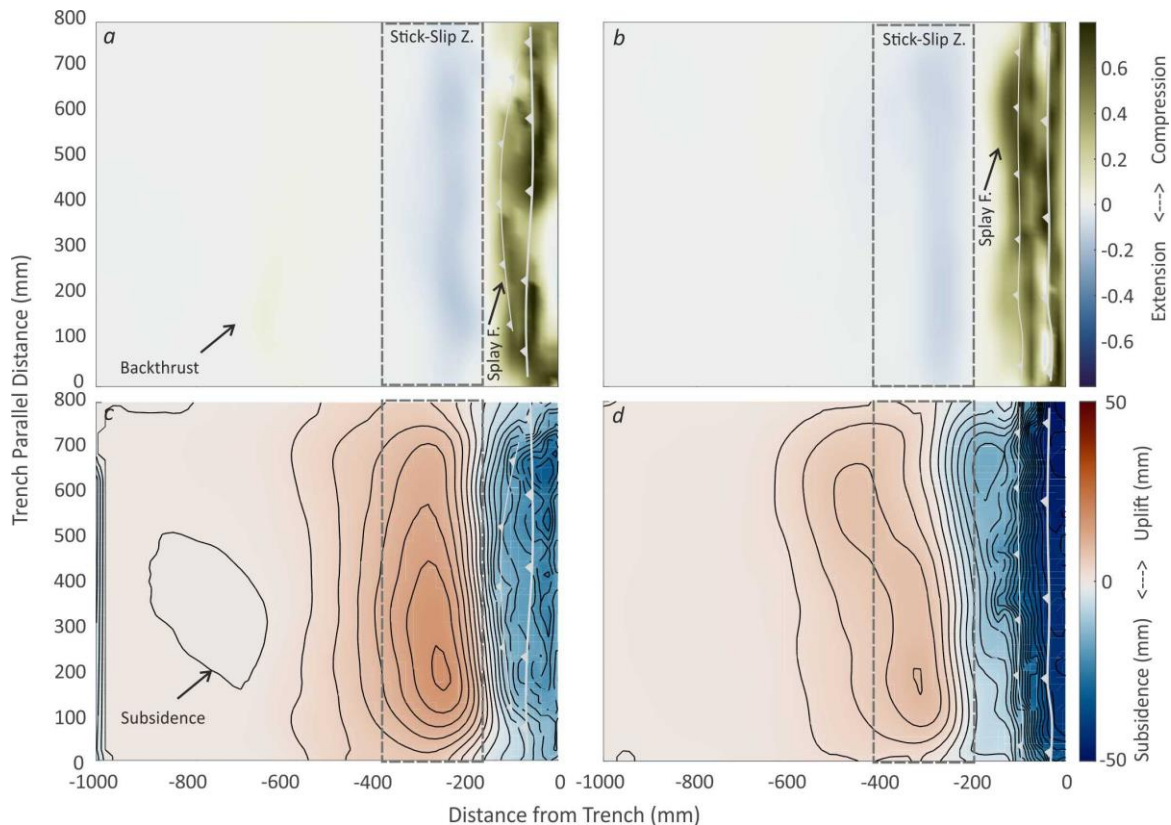
218

219 Figure 5: Final surface topography of compressional (a) and extensional (b) configurations. Backthrust
 220 and the splay faults are rooted in the down-dip and up-dip limit of the stick-slip zone. The splay faults
 221 separate the outer-wedge from the inner-wedge. The strain field generated by the activity of the splay
 222 faults is visualized in c. the ridge-shape structure represents extensional strain. Examples of the surface
 223 coseismic extensional fracture are shown in d and e.

224 Localization of deformation has segmented the upper plate into three main segments. The outer-
 225 wedge is underthrust and subsided. The inner-wedge, which is bounded by the up-dip splay
 226 fault and down-dip backthrust fault, has accumulated the deformation during seismic cycles
 227 through internal deformation and vertical displacement due to the activity of the backthrust
 228 faults. Further rearward (landward), subsidence occurs in the footwall of the backthrust fault
 229 (Figure 6). In the compressional configuration, where the backthrust is developed, the subsiding
 230 area is relatively wider (S1).

231 Both compressional and extensional configurations demonstrate uplift and extension above the
 232 seismogenic zone embraced by shortening domains inland and near the trench. However, the
 233 compressional domain further rearward (onshore) is smaller in the extensional configuration.
 234 Close to the trench, conversely, the upper plate shortens and subsides. In the compressional
 235 configuration, the shortening in the transition zone from the shortening domain to the extension
 236 domain is accommodated by a pop-up structure forming a conjugated forethrust and backthrust
 237 couple. However, the pop-up structure itself generates a local surficial extension domain between

238 its boundary faults (Figure 5). In the extensional configuration, the forethrusts are the only
 239 structures accommodating forearc shortening. In the compressional configuration, the backthrust
 240 fault is the main structure accommodating wedge shortening.



241
 242 Figure 6: Final surface deformation maps from compressional (a and c) and extensional (b and d)
 243 configurations. The approximate location of the stick-slip zone at depth is projected on the model surface
 244 as a dashed rectangle. a and b: Surface strain maps from both configurations. Green and blue represent
 245 compression and extensional domains, respectively. The outer-wedge is experienced (splay fault and
 246 trench domains) compression. Inner-wedge is recorded permanent extension. The activity of the
 247 backthrust is evident in the compressional configurations. c and d: permanent vertical deformation in the
 248 absence of erosion in the system. The outer- and inner-wedge represent permanent subsidence and uplift,
 249 respectively. The slight subsidence zone onshore may represent a forearc basin at the natural scale.

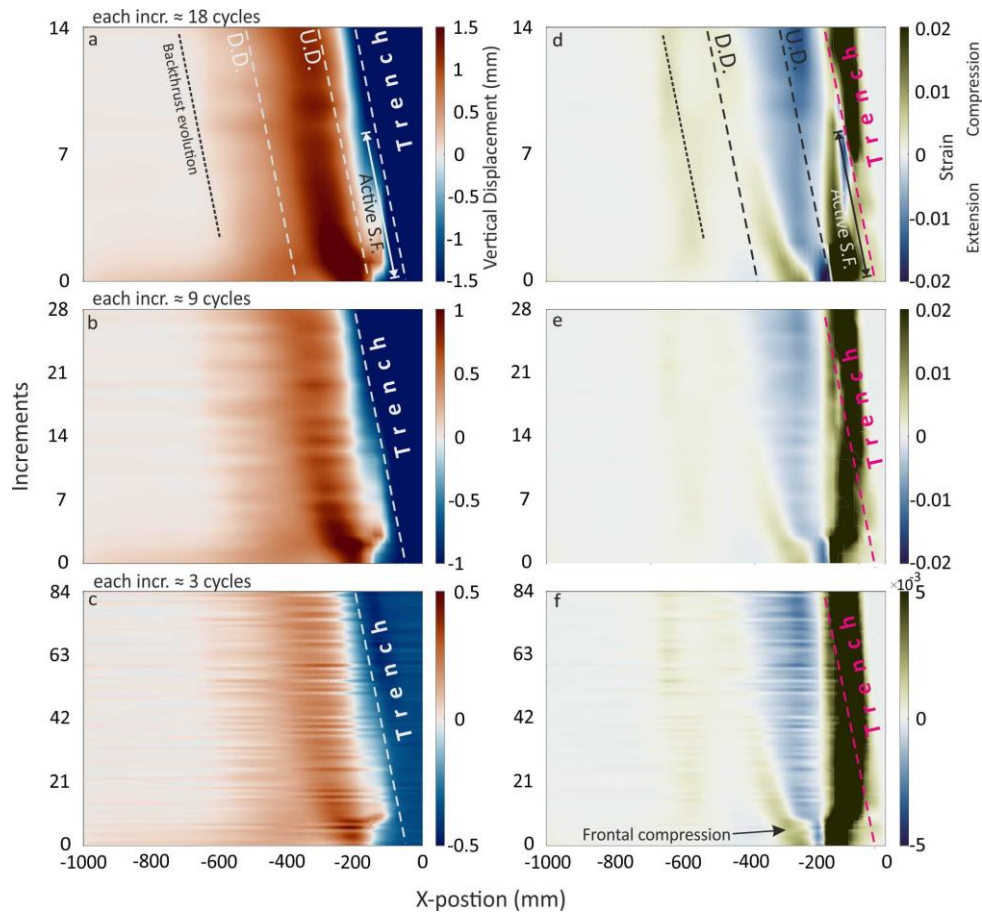
250

251 3.1.2 Upper plate faults evolution over time

252

253 During model evolution, the first structures appear in the vicinity of the deformation front (near
 254 the trench). In the compressional configuration, near the trench, a trenchward-dipping
 255 (backthrust) and a rearward-dipping (forethrust) thrust faults form shortly after each other. These
 256 two trench-parallel faults, likely conjugate at depth, create a ridge-shaped structure (Figure 3).

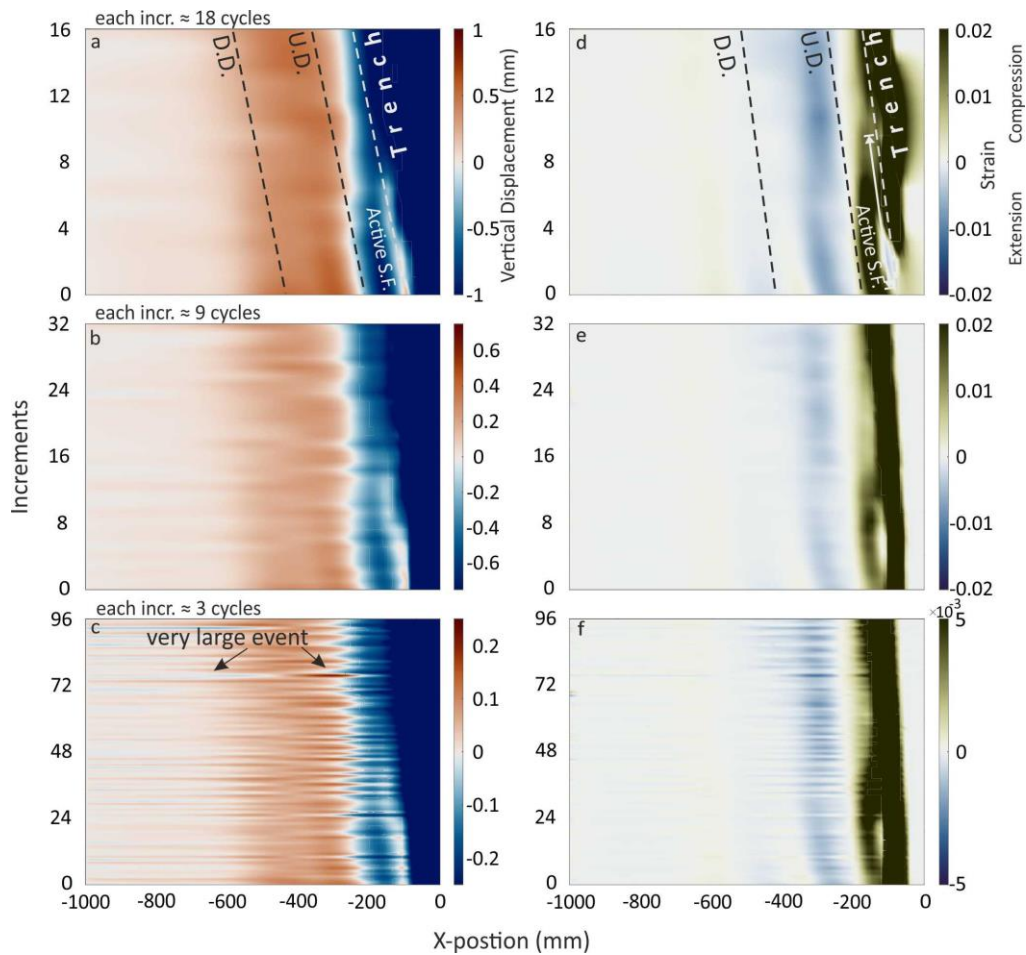
257 The structures



258
 259 Figure 7: Incremental surface vertical displacement and strain over time from the compressional
 260 configuration with different temporal resolutions (3, 9, and 18 analog earthquake cycles). Up-dip (U.D.)
 261 and down-dip (D.D.) of the stick-slip zone at depth have been projected on the surface. a-c represents
 262 vertical uplift (warm color) and subsidence (cold color). The activity of the splay fault (S.F.) is evident
 263 while it is gradually deactivated and the whole slip is transferred on the megathrust. d-f represents surface
 264 strain maps with different temporal resolutions.

265
 266 are formed above the upper basal frictional transition. The stick-slip (seismogenic) zone
 267 represents high basal friction in a long-term (interseismic) interval relative to the interface's
 268 uppermost portion, which creeps interseismically. This frictional contrast thus leads to a sharp
 269 slip rate variation and stress concentrations along the interface where thrusts nucleate. Another
 270 active trenchward-dipping thrust fault (backthrust) forms further rearward in the wedge,
 271 representing the onshore segment of the forearc. Again, the frictional contrast between the
 272 velocity weakening portion of the interface (seismogenic zone) and the downdip limit of this

273 portion controls the origin of the backthrust, thereby accommodating the difference in slip rate
 274 (Figures 5 and 6). The thrust



275
 276 Figure 8: Incremental surface vertical displacement and strain over time from an extensional
 277 configuration with different temporal resolutions (3, 9, and 18 analog earthquake cycles). Up-dip (U.D.)
 278 and down-dip (D.D.) of the stick-slip zone at depth have been projected on the surface. a-c represents
 279 vertical uplift (warm color) and subsidence (cold color). The activity of the splay fault (S.F.) is evident
 280 while it is gradually deactivated and the whole slip is transferred on the megathrust. d-f represents surface
 281 strain maps with different temporal resolutions.

282
 283 system accommodates shortening, causing uplift and steepening of the wedge over the course of
 284 the experiment consistent with the predicted transiently compressional initial geometry.
 285 In the extensional configuration, a splay forethrust forms at the up-dip limit of the seismogenic
 286 zone (Figure 3). In contrast to the compressional wedge, a backthrust does not form at the
 287 downdip limit of the seismogenic zone consistent with its stable geometry according to Coulomb

288 wedge theory. These faults show thrust mechanisms and form in the immediate up-dip and
289 down-dip parts of the seismogenic zone.

290

291 **3.1.3 Long-term wedge deformation: Long-term surface displacement signals reflecting** 292 **forearc evolution.**

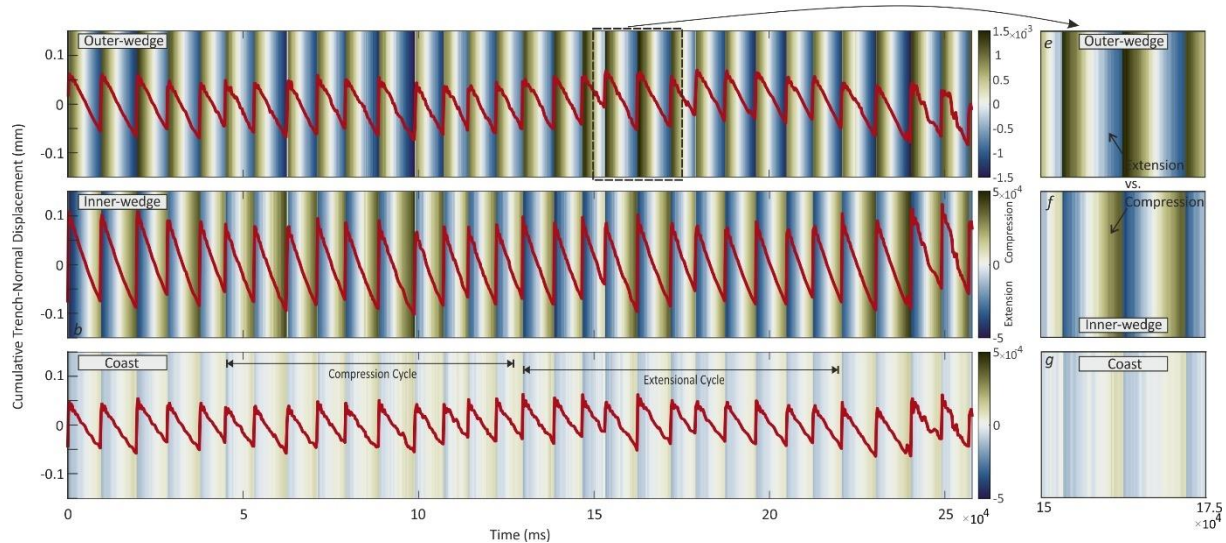
293

294 To visualize the long-term behavior (i.e., integrating multiple seismic cycles) of the models,
295 forearc wedge differential surface displacement (horizontal and vertical) of increments lasting
296 150, 75, and 25 seconds are plotted. This covers about 18, 9, and 3 megathrust analog earthquake
297 cycles, respectively (Figures 7 and 8), to illustrate how the wedge evolution is recorded by
298 observational data with different temporal resolutions typical of geomorphological methods (e.g.,
299 terrace uplift).

300 In both configurations, the long-term vertical displacement can be temporally divided into two
301 parts depending on whether the upper plate faults are active or inactive. In the case of an active
302 splay fault, the horizontal trenchward displacement terminates at the location of the splay fault
303 (Figure 4), and the zone of maximum uplift is in the hanging-wall of the splay fault (Figures 7
304 and 8). The splay fault activity decreases over time until it dies, and subsequently, the whole slip
305 is consumed on the interface (i.e., megathrust). Namely, a non-trench-reaching megathrust
306 earthquake system turns into a trench-reaching system over time. The evolution of the backthrust
307 can also be tracked in all temporal resolutions of topography evolution derived from the
308 compressional configuration (Figure 7). The zone of maximum topography correlates with the
309 zone of the maximum extensional segment of the upper plate in both configurations. In the
310 compressional configuration, this extensional zone becomes wider and more pronounced over
311 time, while the width of the zone remains relatively constant over time in the extensional
312 configuration.

313 Further rearward to the coastal region, the strain evolves differently in the compressional and
314 extensional configurations: In the compressional configuration, the initially extensional strain is
315 replaced by a compressional domain over the entire inner-wedge. The maximum compressional
316 strain appears in the coastal region where the backthrust is formed. The frontal compressional
317 domain diminishes while the compressional wedge is evolving. This is in good agreement with
318 the activity of the up-dip splay fault over its lifetime. The strain pattern over the inner-wedge
319 illustrates that this wedge segment gradually evolves to a more compressional regime. In
320 contrast, there is no significant frontal compressional domain in the extensional configuration

321 (Figure 8), and the inner-wedge is rather in an extensional state. Although the coastal region in
 322 the extensional configuration similarly shows a compressional state, the backthrust fault does not
 323 appear in the wedge at the down-dip limit of the stick-slip zone.



324
 325 Figure 9: Compressional configuration; Trench-normal displacement time-series (red plot) is overlaid
 326 on the strain time-series (background color map) over tens of analog earthquake cycles in different
 327 segments of the upper plate. The magnitude of the strain in the outer-wedge is one order larger than the
 328 inner-wedge and coast. Note that the outer- and inner-wedge show opposite strain state over the
 329 earthquake cycle (compressional versus extensional). The compression and extensional supercycles in the
 330 coastal region are shown in the lower panel. Please see the text for the discussion.

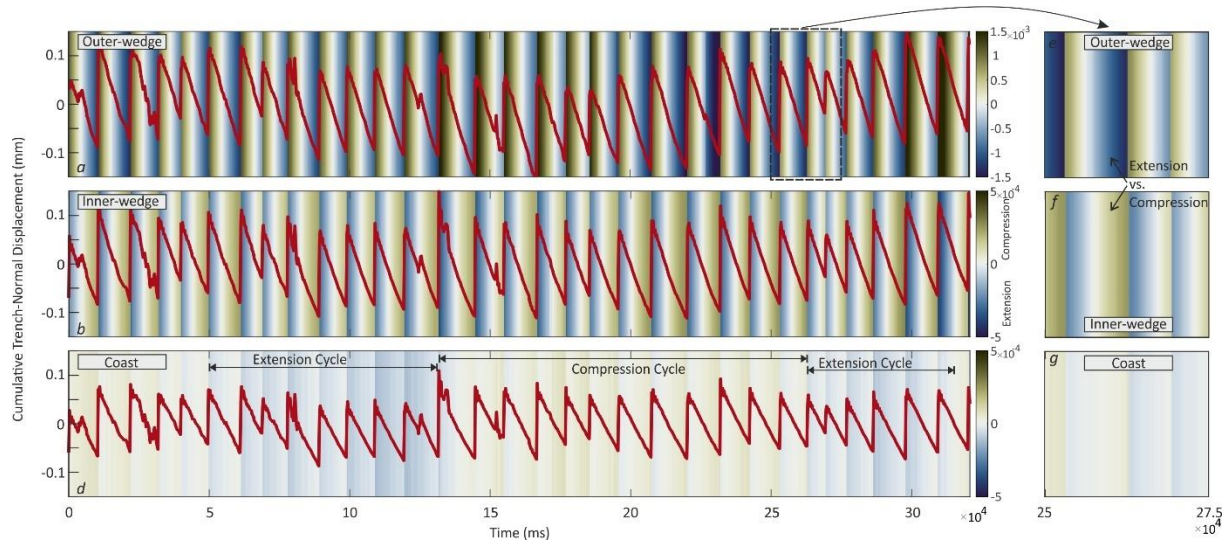
331 3.1.4 Short-term wedge deformation: Strain pattern over seismic cycles

332 3.1.4.1 Extensional features in the shallow segment of the forearc

333 The extensional features have generally been observed as extensional fractures or/and crestal
 334 normal faults in the frontal wedge domain of the models (Figure 5 and S2). The latter may form
 335 above the frictional transition zone at the up-dip limit of the velocity-weakening zone. The
 336 activity of the forethrust splay faults plays the main role in their formation being located in the
 337 crestal zone in the hanging-wall of the splay fault. This fracture zone reflects the splay fault's
 338 activity and, consequently, the up-dip limit (frictional transition) of the velocity-weakening
 339 portion of the interface. The extensional features form and develop trench-parallel inelastically
 340 over the interseismic interval and are active in opposite modes during the coseismic and
 341 postseismic stages, i.e. coseismically extensional and postseismically compressional. The
 342 responsible formation mechanism is the splay forethrust the activity of which generates fault-

343 related folds (fault-propagation fold) (S2).

344 Consequently, a local extensional regime forms at the hinge zone of the fault-related fold and
 345 may lead to the crestal normal faults. In the coseismic interval, a sudden slip on the splay fault
 346 and megathrust enhances these extensional fractures. The slip on the faults terminates at the
 347 frictional transitional border. Hence, a compressional strain regime appears in the forelimb of the
 348 fault-related fold.



349 Figure 10: Extensional configuration; Trench-normal displacement time-series (red plot) is overlaid on
 350 the strain time-series (background color map) over tens of analog earthquake cycles in different segments
 351 of the upper plate. The magnitude of the strain in the outer-wedge is one order larger than the inner-
 352 wedge and coast. Note that the outer- and inner-wedge show opposite strain state over the earthquake
 353 cycle (compressional versus extensional). The compression and extensional supercycles in the coastal
 354 region are shown in the lower panel. Please see the text for the discussion.

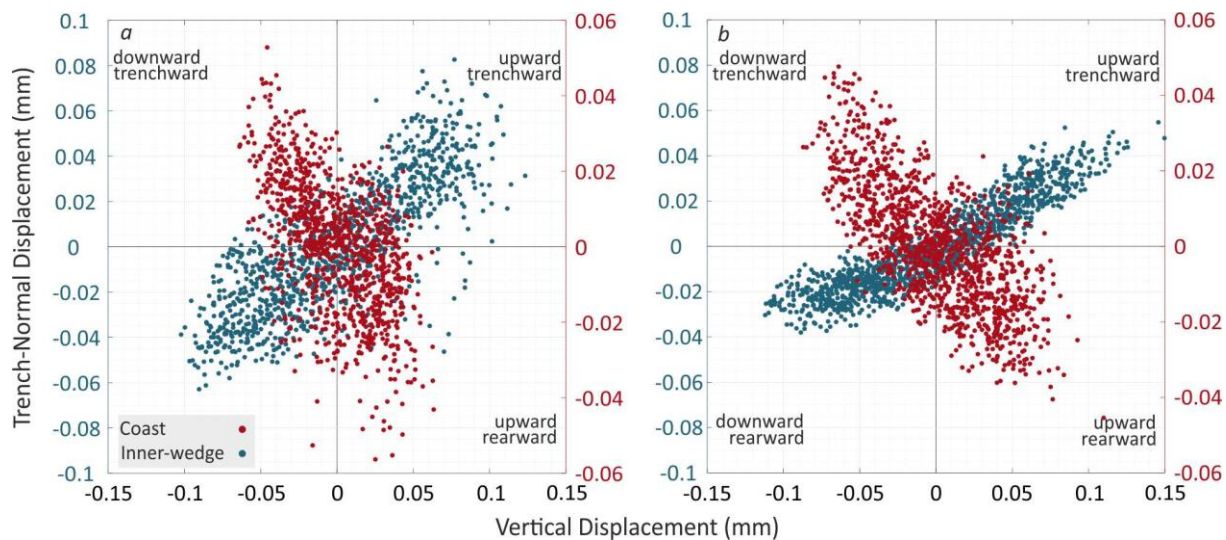
356 The fractures appear in the inner-wedge segment of the model forearc where they overly the
 357 velocity-weakening portion of the interface at depth. The extensional fractures in the inner-
 358 wedge above the seismogenic zone form coseismically where the maximum extensional strain
 359 occurs in the forearc and is partially preserved as anelastic deformation (i.e., normal faulting) in
 360 the inner-wedge in each earthquake cycle. In contrast, during the interseismic period, this
 361 segment of the forearc is mainly under compression.

362 3.1.4.2 Strain-state cycle over the seismic cycle

363 Here we have visualized the average value of the strain over three different segments of the
 364

365 upper plate forearc to take a closer look at the strain evolution at the timescale of individual
 366 seismic cycles (Figures 9 and 10). In general, the strain rate reduces rearward from the trench
 367 toward the coast, consistent with the dominance of elastic loading at the seismic cycle timescale.
 368 The outer-wedge shows strains opposite to those of the coast and inner-wedge (Figures 9 and
 369 10). The inner-wedge and coast are under compression when the outer-wedge is experiencing
 370 extension during the interseismic period—this is a general pattern over many seismic cycles. In
 371 each cycle, the inner-wedge undergoes extension coseismically, then gradually moves to a
 372 neutral state and finally shifts to a stably compressional state and stays in this regime until the
 373 next seismic event occurs. In contrast, the outer-wedge is under compression during the
 374 earthquake and subsequently experiences neutral and extensional states in the interseismic
 375 interval. In both segments, the strain state shows a regular cycle and follows the same earthquake
 376 cycle trend.

377



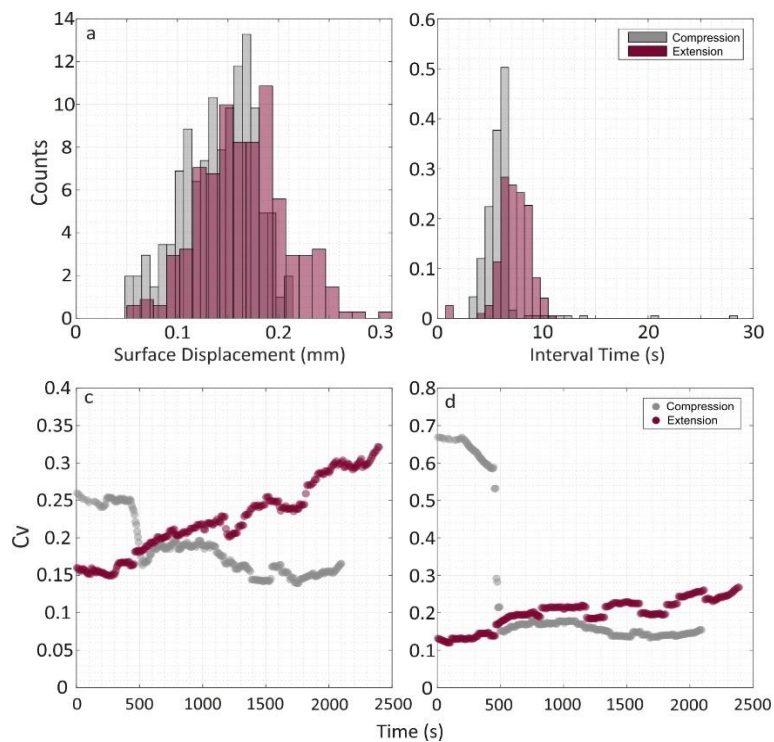
378

379 Figure 11: Comparison between surface displacements (horizontal and vertical) in the inner-wedge and
 380 coast segments. The segments demonstrate opposite trends: the coast moves trenchward while subsiding
 381 (and vice versa), but the inner-wedge moves trenchward while moving upward.

382 In the down-dip segment, which is treated as underlying the coastal area in our experiment (cf.
 383 Fig. 1), the strain state cycle differs from that of the two shallower (offshore) segments of the
 384 upper plate. Although the strain magnitude is approximately an order of magnitude smaller, its
 385 pattern may be closer to the inner-wedge than to the outer-wedge.

386 Interestingly, the strain state represents not only an asymmetric cyclic pattern over stick-slip

387 cycles but also a longer cycle (hereafter called “supercycle”) (Figures 9 and 10). In the coastal
 388 segment, unlike the other upper plate segments, the extensional and compressional portions of
 389 the strain do not balance over a few cycles but show multi-cycle long compressional and
 390 extensional supercycles. The supercycle appears sharper in the extensional configuration, where
 391 the backthrust is not developed. It may, therefore, be due to the activity of the backthrust that
 392 perturbs the supercycle. The surface displacements in the coastal zone and the inner-wedge
 393 represent opposite trends (Figure 11). In the coseismic period, the coast, which overlies the
 394 down-dip limit of the stick-slip zone, moves trenchward while subsiding (and vice versa in the
 395 interseismic period), but the inner-wedge, which overlies the stick-slip zone, moves trenchward
 396 while moving upward. This implies that coseismic uplift and subsidence patterns indicate the
 397 location of the slipped zone at depth. The possible primary mechanisms for the supercycle will
 398 be discussed in the discussion.
 399



400

401 Figure 12 : Size and frequency distributions (a and b) and coefficients of variation (Cv) of recurrence
 402 intervals and size (c and d) of analog megathrust events for compressional and extensional
 403 configurations.

3.2 Frequency and size distributions of analogue megathrust events

To explore the possible relationship between moment release patterns and forearc configurations, we compare the frequency and size of analog megathrust events and their coefficients of variations (C_v). This coefficient is defined as the ratio of the mean to the standard deviation of the data, from both compressional and extensional configurations (Kuehn et al., 2008; Rosenau & Oncken, 2009). We have defined a moving window to calculate the coefficient of variation over the size and frequency of events. The coefficient of variation generally exhibits an inverse relationship (i.e., negative correlation) with the periodicity of the frequency-size distribution. In particular, a C_v of 1 indicates random events while a $C_v < 0.5$ characterizes periodic events.

The results of the size and frequency distribution and temporal evolution of the frequency-size distributions are plotted in figure 12. Accordingly, the extensional configuration is characterized by relatively larger event size and longer recurrence. In the C_v plots of the compressional configuration (Figure 12 c and d), a sharp reduction is clear. Its timing shows a good agreement with the evolution of the main upper plate structures (i.e., backthrust fault). The C_v of the compressional configuration is generally lower than that of the extensional configuration, indicating that the first is more periodic. Although both configurations demonstrate rather periodic behavior (i.e. $C_v < 0.5$), the recurrence pattern of the extensional configuration, unlike the compressional configuration, evolves over time towards higher variability. The C_v values for the extensional configuration systematically increase and are characterized by a C_v higher than 0.15. In contrast, in the compressional configuration, the values stay in a range of 0.15-0.2. A similar trend is also observed in the size distributions of both models. The compressional configuration does not show a significant evolution over time; however, an increasing trend is observed towards higher coefficients (i.e., less characteristic events over time) in the extensional configuration.

4 Discussion

4.1 Mechanical state of the shallow forearc over the seismic cycle

We have used critical wedge theory to design two endmember wedge geometries to see the effect of (transient) instability on the long-term deformation pattern. As shown in figure 2, the wedge is

436 predicted to be critically compressive and stable during the interseismic and coseismic periods,
437 respectively, in the compressional configuration. In the extensional configuration, the onshore
438 and offshore segments of the wedge represent different states: In the coseismic period, the
439 offshore segment, unlike the onshore segment, is prone to be critically extensional. The offshore
440 segment is stable in the interseismic period, but the onshore segment tends to be critically
441 compressional.

442 The outer-wedge segment of our model overlies the creeping portion of the interface where slip
443 instability cannot nucleate but may rupture during trench-reaching megathrust events (Cubas et
444 al., 2013a; Noda and Lapusta, 2013). This domain is near the deformation front and undergoes
445 more deformation and splay thrust faulting than the other forearc segments. This segment
446 switches its stability state from compressional critical in the interseismic stage to a coseismically
447 stable condition. Analog earthquake studies suggest that a mega-splay fault at the up-dip limit of
448 the velocity-weakening zone may act as a relaxation mechanism for coseismic compression
449 (Rosenau et al., 2009) and be activated in the early postseismic stage of a seismic cycle. These
450 laboratory observations are in good agreement with the aftershock activities after megathrust
451 events, for instance, after the Maule 2010 (Lieser et al., 2014), Antofagasta 1995 (Pastén-Araya
452 et al., 2021), Iquique 2014 (Soto et al., 2019), and Ecuador–south Colombia 1958 earthquakes
453 (J.-Y. Collot et al., 2008; Jean-Yves Collot et al., 2004). This implies that coseismic
454 strengthening of the shallow megathrust pushes the outer-wedge to a compressively critical state
455 during large displacements on the interface (Figure 10) (Hu & Wang, 2008; Wang et al., 2019;
456 Wang & Hu, 2006). Consequently, the splay fault between the outer and inner-wedge may
457 accumulate slip during coseismic or/and postseismic periods.

458 The inner-wedge is located between this forethrust splay fault and the projection of the down-dip
459 limit of the stick-slip zone to the surface or the backthrust upper-plate fault (Figure 5). This
460 segment is interseismically stable and a minimum of permanent deformation is accumulated
461 (Cubas et al., 2013b). The maximum strain is localized on the backthrust fault which is the
462 landward boundary of the inner-wedge. However, this backthrust may activate with a normal
463 faulting mechanism during or immediately after a large coseismic slip in the velocity-weakening
464 portion of the interface, similar to the activity of the Pichilemu fault shortly after the Maule 2010
465 megathrust earthquake (Farías et al., 2011; Cubas et al., 2013b). This means that the
466 mechanically most stable segment of the entire wedge – i.e. the inner wedge - reflects the

467 seismically most active (i.e., velocity-weakening) portion of the interface. (Fuller et al., 2006).

468

469 **4.2 Seismotectonic forearc segmentation: Comparison with natural examples**

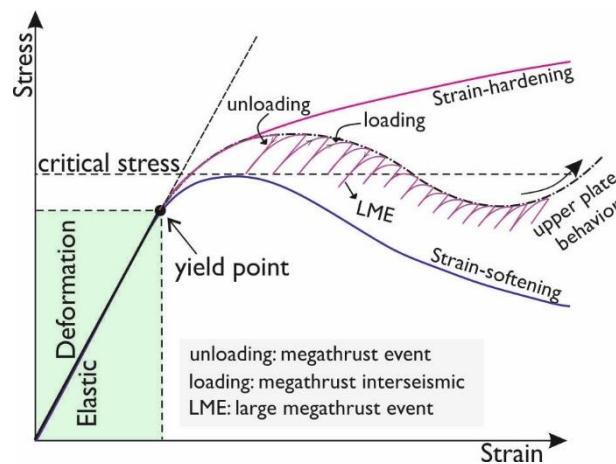
470 Our results highlight how coseismic surface deformation may contribute to the morphology of
471 the shallow (offshore) segment of the forearc. The coseismic extension that occurs offshore is
472 mainly observed in the inner-wedge, in the zone bounded by the up-dip forethrust (and/or
473 backthrust) and down-dip backthrust (Figures 5). The up-dip forethrust is the same structure that
474 has been observed in several natural examples. It has been introduced as either backstop in the
475 2011 Tohoku-Oki earthquake region in the Japan Trench (Ito et al., 2011; Tsuji et al., 2011,
476 2013) or as the approximate limit between the lower and middle slopes (MLS) in the north
477 Chilean margin (Maksymowicz et al., 2018; Storch et al., 2021). In the former, the fault is
478 characterized by the boundary between a soft and fractured sediment sequence abutting a less-
479 deformed sequence on the landward side. After the 2011 Tohoku-Oki event, seafloor
480 photographs taken from the splay fault (backstop) region show that extensional steep cliffs are
481 formed coseismically due to small-scale slope failure (Tsuji et al., 2013). We observe similar
482 gravity-induced features in the forelimb of the splay fault in our experiments, indicating the up-
483 dip limit of the coseismic slip on the interface. Further landward, seafloor photographs from the
484 inner-wedge have suggested coseismic anelastic extensional features with no evidence for
485 submarine landslides and reverse faulting as responsible mechanisms (Tsuji et al., 2013). This
486 segment of the upper plate in both our models and the 2011 Tohoku-Oki event overlies the zone
487 of maximum coseismic slip.

488 Seafloor extensional features have also been documented in the regions of the Maule 2008 and
489 Iquique 2014 earthquakes in the central and northern Chilean subduction zone (Geersen et al.,
490 2016, 2018; Maksymowicz et al., 2018; Reginato et al., 2020; Storch et al., 2021). A normal
491 faulting escarpment and extensional fractures are observed on the hanging wall of the forethrust
492 splay in the Maule 2008 earthquake region (Geersen et al., 2016). Although it is not evident
493 whether the normal faults are rooted in the megathrust interface, the extensional fractures on the
494 hanging wall may be related to the activity of the splay fault. As shown in our model's results,
495 the activity of the splay fault at the up-dip limit of the rupture area may generate an extensional
496 regime in the hinge zone of the fault-related fold and forms extensional fractures. Note that these
497 frontal splay faults may be active during earthquakes and/or in postseismic intervals. In both
498 cases, however, they indicate the frictional transition zone on the plate interface and, in

499 consequence, the up-dip limit of the locked seismogenic zone. In line with our model result, the
 500 extensional basin between the splay fault (backstop) and coastal region indicates the megathrust
 501 seismogenic zone at depth (Moscoso et al., 2011). The large subduction earthquakes may rupture
 502 different portions of the interface from the trench to the downdip end of the seismogenic zone
 503 (Lay et al., 2012). Depending on the earthquake magnitude and position of the ruptured segment
 504 (i.e., the portion of the megathrust interface beneath the coastal region), the extensional fractures
 505 can also be seen onshore as a marker of permanent deformation (Baker et al., 2013; Loveless et
 506 al., 2005, 2009).

507 In the Iquique 2014 earthquake region (North Chilean subduction system), clear evidence of the
 508 extensional features in the upper plate has been reported from offshore seismic profiles (Geersen
 509 et al., 2018; Reginato et al., 2020; Storch et al., 2021). The offshore extensional features can be
 510 categorized into two domains, the Middle-Lower slope transition (MLS), and Middle-Upper
 511 slope segments. The former is likely formed by the activity of the large forethrust splay, which
 512 may be active during co-, post-, and interseismic intervals. The Middle-Upper slope segment
 513 overlies the main slip zone of the 2014 event. It is possibly formed coseismically and generates
 514 the sedimentary basin over hundreds of seismic cycles. This latter correlation also correlates with
 515 the gravity anomaly (Schurr et al., 2020) introduced by (Song & Simons, 2003; Wells et al.,
 516 2003).

517



518

519 Figure 13: A suggested scenario for the coastal segment of the upper plate behavior over tens of seismic
 520 cycles. After exceeding the elastic domain, the upper plate at the location of the coast goes to the strain-
 521 hardening domain over a few seismic cycles and then moves towards the strain-softening domain. The

522 pulses of megathrust events (loading and unloading) accelerate this switch from strain-hardening to
523 strain-softening.

524 **4.3 Forearc segmentation and temporal pattern of events**

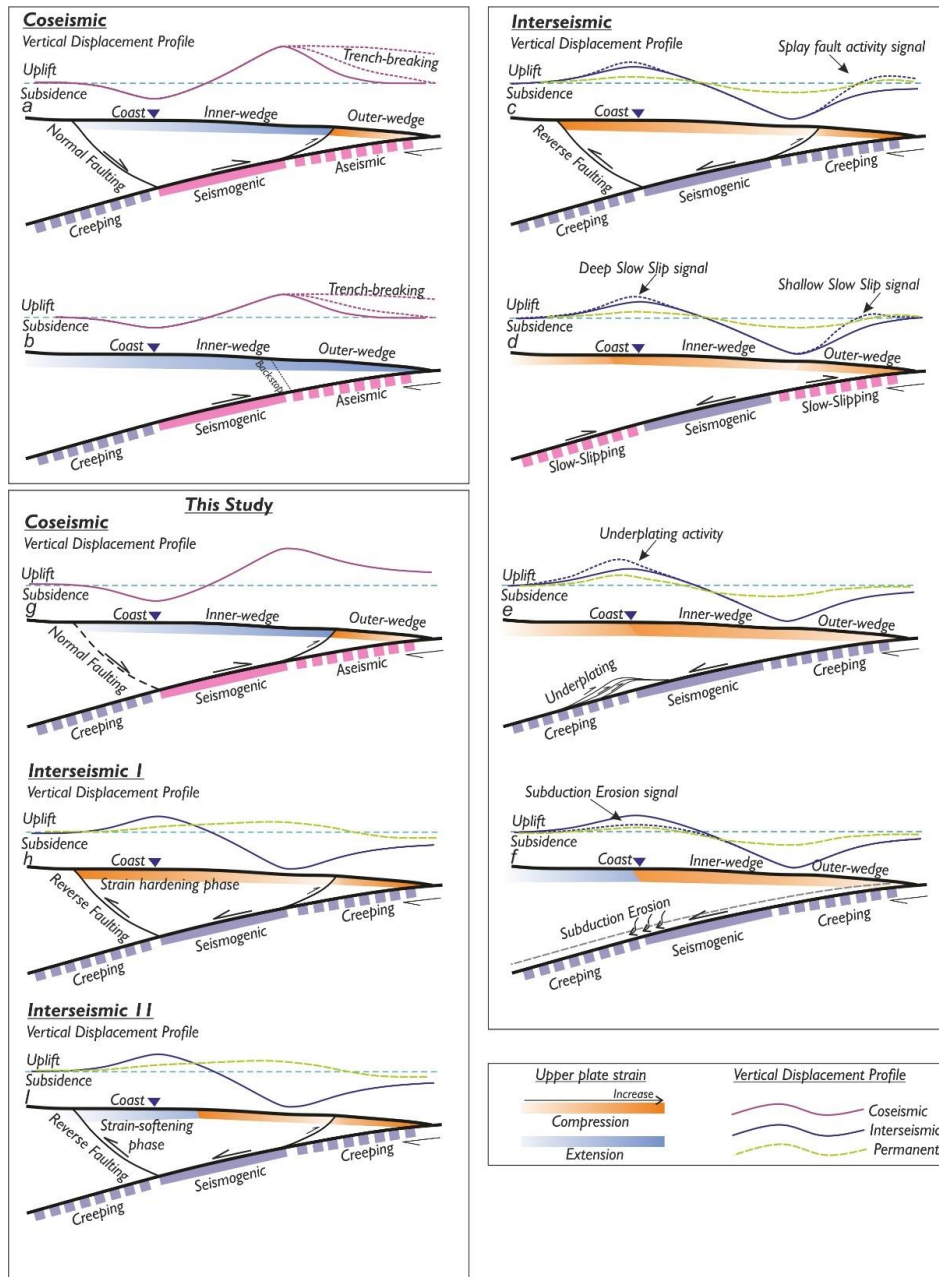
525
526 The compressional configuration establishes a clear forearc segmentation through forming up-
527 dip (offshore) splay faults and down-dip (onshore) backthrust faults, causing the analog
528 megathrust events to be more regular (same evolution as in Rosenau and Oncken, 2009). Lacking
529 a backthrust, the extensional wedge does not have this clear segmentation, causing more
530 irregular analog megathrust events. However, both are still generally periodic, i.e. $CV < 0.5$.
531 Moreover, the forearc segment bounded by the upper plate faults overlies the seismogenic zone;
532 hence, the frontal shortening segment (i.e., inner-wedge) of the compressional configuration
533 behaves as a deterministic spring-slider system (Reid, 1910; Rosenau & Oncken, 2009). In the
534 extensional configuration, the extensional fractures on the segment above the seismogenic zone
535 indicate anelastic deformation that correlates with a more complicated temporal pattern of the
536 megathrust events. This is equivalent to the observation of a less periodic pattern of analog
537 earthquakes produced in the extensional configuration.

538 **4.4 Coastal strain cycle in response to earthquake cycle**

539 In our model, the projection of the downdip limit of the velocity weakening zone on the surface
540 represents the coastal region (Oleskevich et al., 1999; Ruff & Tichelaar, 1996). Unlike the inner-
541 wedge and outer-wedge, the coastal region reacts in an inhomogeneous pattern to the seismic
542 cycles: its strain state does not only respond to each event (i.e., megathrust earthquake), but the
543 strain state shows a “supercycle” over several cycles. In other words, a “strain-switch” from
544 compressional/extensional to an extensional/compressional state develops over a few cycles
545 (Figures 9 and 10). We hypothesize that internal deformation in the experimentally well-known
546 elastoplastic deformation cycle may be the responsible mechanism for the supercycle. The strain
547 rate in the coastal domain is at least one order of magnitude lower than that in the offshore
548 forearc segments; hence, the onshore segment needs more time to reach its yield strength and to
549 shift between strain-hardening and strain-softening periods.

550 On the other hand, a stress transfer caused by a megathrust earthquake perturbs this process and
551 accelerates/decelerates the deformation rate. When the coastal area is in a strain-hardening
552 period, megathrust coseismic pulses gradually push it toward a neutral stage approaching failure
553 and the resultant switch to strain-softening. However, a very large coseismic pulse may also

554 quickly drag it into the strain-softening domain. After the coseismic event, the coast again moves
555 toward the strain-hardening regime (Figure 13). These changes in the strain cycles reflect
556 variability in strain rate with respect to the long-term trend such that the compressional wedge is
557 more segmented, its deformation varies less compared to the unsegmented extensional wedge.
558 Observations reveal that a relatively low resolution (18 cycles in this case) may provide a good
559 overview of the wedge evolution type as outlined above. However, the details of the cycles and
560 the transient in between may be overprinted, for example, by the supercycle-related
561 uplift/subsidence and megathrust events involving splay faults. The comparison suggests that the
562 seismic cycle-to-cycle variability causes periodicity in the surface deformation at all
563 (observational) frequencies. The Northwest Coast of the Tohoku-Oki 2011 earthquake (NE
564 Japan; Japan trench) and the Pacific coast of Hokkaido (Kuril trench) have both experienced two
565 different long-term vertical movement histories. In the former case, the Pleistocene marine
566 terrace



567
568 Figure 14: Schematic of vertical displacement and strain state during the coseismic period and
569 interseismic interval in different segments of upper plates for different scenarios. Note that we assume the
570 coast reflects the down-dip limit of the seismogenic zone at depth; modified after (Clark et al., 2019;
571 Farías et al., 2011; Herman & Govers, 2020; Madella & Ehlers, 2021; Melnick et al., 2018; Menant et al.,
572 2020; Moreno et al., 2009; Mouslopoulou et al., 2016; Ozawa et al., 2011; Rosenau & Oncken, 2009;
573 Simons et al., 2011; Sun et al., 2017; Wang et al., 2019; Wang & Tréhu, 2016, and many others).

574

575

576 chronology of the NE coast of Japan has experienced a constant uplift at about 0.2 m/ky.
577 (Matsu'ura et al., 2019). In contrast, the Holocene sedimentary succession in the south and
578 central Sanriku suggests subsidence at about 1 mm/yr. (Niwa et al., 2017). If this opposite long-
579 term coastal vertical movement is accurate enough, it may reflect the coastal strain supercycle in
580 response to the megathrust cycle. In the latter case, the sedimentological investigations and
581 diatom assemblages suggest pre-seismic submergence at a rate of 8–9 mm/yr. (Atwater et al.,
582 2016; Sawai, 2020; Sawai et al., 2004). If this rapid subsidence occurs in each earthquake cycle,
583 megathrust coseismic and postseismic deformation should generate 4–5 m of coastal uplift in
584 each cycle to cancel out the subsidence. A similar subsidence-uplift pattern also accrued in the
585 Aleutian-Alaska subduction system (Shennan & Hamilton, 2006).

586 The above inconsistency in vertical movement of the coast occurs in subduction systems where
587 the megathrust earthquake usually ruptured the offshore (i.e., shallow) part of the interface (e.g.,
588 Japan and Alaska trenches) (Figure 14). In the cases where the megathrust earthquakes that
589 partially or fully ruptured the deep part of the interface, for instance, the Antofagasta 1995
590 (Chlieh et al., 2004; Pritchard et al., 2002) and Illapel 2015 earthquakes (Tilman et al., 2016),
591 marine terraces recorded a more continuous uplift (with different rates) since the Pleistocene
592 (González-Alfaro et al., 2018). However, a long-term (Miocene) change in the vertical
593 movement has been recorded in some places on the Coastal Cordillera in the Chilean margin,
594 probably caused by basal erosion/accretion sequences (Encinas et al., 2012). This may imply that
595 if the coastal area subsides coseismically but uplifts over the interseismic period, the coast
596 probably overlies the downdip limit of the locked zone while the coastal region may show long-
597 term vertical movement inconsistently. If the coast moves vertically upward during both
598 coseismic and interseismic periods, upper plate thrust faults likely push the coast upward (Clark
599 et al., 2019; Mouslopoulou et al., 2016) and the coastal region continuously accumulates
600 permanent uplift.

601 Deep slow-slip events, basal accretion, interseismic crustal thickening, and upper plate faulting
602 may enhance coastal uplift at different time scales (Figure 14). Among these processes,
603 underplating may not play a significant portion in a single seismic cycle because the formation of
604 each tectonic slice (i.e., duplex) is in a Myr-scale (Menant et al., 2020; Ruh, 2020). The thermo-
605 mechanical simulations (Menant et al., 2020) suggest early and late stages of a single
606 underplating cycle respectively characterized by up to 1.5 mm/yr. uplift and subsidence (i.e., re-

607 equilibration of the forearc wedge) rate in the coastal region. This transition from uplift to
 608 subsidence (and vice versa) is in the Myr-scale and represents a much lower frequency in
 609 comparison with the deformation supercycle observed in our experiments. However, to rule out
 610 and differentiate the impact of the different mechanisms involved in the vertical movement of the
 611 coastal region, a modeling approach including all the above-mentioned mechanisms is needed.

612

613 Table 1: Summary of short- and long-term forearc strain state

Configuration	Compressional config.	Compressional config.	Compressional config.	Extensional config.	Extensional config.	Extensional config.
Forearc segment	<i>Coseismic</i>	<i>Interseismic</i>	<i>Long-term permanent</i>	<i>Coseismic</i>	<i>Interseismic</i>	<i>Long-term permanent</i>
outer-wedge	Compression	From compression moves to a neutral state and finally to extension	Compression	Compression	From compression moves to a neutral state and finally to extension	Compression
Inner-wedge	Extension	From extension moves to a neutral state and finally to a stably compressional	Extensional; extensional zone becomes wider over time	Extension	From extension moves to a neutral state and finally to a stably compressional	Extensional over the seismogenic zone; surface extensional fractures
Coastal region	Extension	Extensional & compressional portions do not balance; asymmetric cyclic pattern	Multi-cycle long compressional/extensional supercycles	Extension	Extensional & compressional portions do not balance; asymmetric cyclic pattern	Multi-cycle long compressional/extensional supercycles; sharper supercycle

614

615

616 Although the inner-wedge and outer-wedge may show a relatively simple earthquake
 617 deformation cycle, the coastal zone in the subduction zones may also show a rather complicated
 618 pattern and trend. Where the downdip limit of seismic locking and slip is offshore, both, the
 619 deformation resulting from seismic cycle deformation and that from mass flux at the plate
 620 interface (subduction erosion vs. underplating) generate a composite, more complex kinematic
 621 record, even in our simplified seismotectonic model. This implies that predicting the interface
 622 behavior from the coastal behavior might not always provide diagnostic evidence in the case of
 623 shallow subduction earthquakes where the coast does not overlie the seismogenic zone or its
 624 downdip end. Rather, measuring surface deformation above the locked zone provides a more
 625 reliable indication of the behavior of the interface.

626 **5 Conclusion**

627

628 Our results highlight that, in the shallow portion of the subduction zone, frictional properties of
 629 the interface and mechanical characteristics of the forearc determine the surface deformation

630 signal over seismic cycles. The mechanical and kinematic interaction between the shallow wedge
631 and the interface can partition the wedge into different segments. These segments may react
632 analogously or oppositely over the different intervals of the seismic cycle (Table 1). Moreover,
633 different wedge segments may switch their strain state from compression/extension to
634 extension/compression domains. We emphasize that a more segmented upper plate is related to
635 megathrust subduction that generates more characteristic and periodic events.

636 Our experiments underscore that the stable part of the wedge (i.e., inner-wedge) which
637 undergoes extension coseismically overlies the seismogenic zone. However, the density of
638 extensional fractures and the number of normal faults may increase toward the limit between the
639 inner-wedge and outer-wedge due to the activity of splay faults at the up-dip limit of the
640 seismogenic zone.

641 Over a dozen and more analog earthquake cycles, the strain time series reveal that the strain
642 state may switch the mode after remaining quasi-stable over a few seismic cycles in the coastal
643 zone. Various scenarios have been suggested, such as background seismicity, deep slow-slip
644 events, subduction accretion/erosion, as the responsible mechanism for switching the kinematic
645 behavior of the coastal domain (uplift to subsidence and vice versa). Here we additionally show
646 that the mechanical state of the plate interface beneath the coastal region, may vary over time
647 and influence the coastal region strain state. Because the strain rate here is significantly lower
648 than in the offshore segment, this may eventually lead to different observed vertical motions on
649 the coast. Megathrust events might be a driving agent that accelerates the strain state switch and
650 pushes the coastal region from a strain-hardening to strain-softening state. Our simplified
651 experiments demonstrate that the strain cycle in the coastal region may show a supercycle pattern
652 superseding sawtooth pattern of the strain cycles related to the earthquake cycle. This is
653 geodetically relevant as the observations in many subduction zones are focused in the coastal
654 regions. Hence, it may not always be straightforward to use these observations as direct evidence
655 to assess the behavior of the shallow, offshore portion of the megathrust.

656

657 **Data Availability Statement**

658 All data in this study will be published open access soon (data archiving is underway). We thank
659 GFZ Data Services for publishing the data. Meanwhile, the data set is uploaded as Supplemental
660 Material for review purposes.

661
662
663
664
665
666

Acknowledgment

667 The research is supported by the SUBITOP Marie Skłodowska-Curie Action project from the
668 European Union's EU Framework Programme for Research and Innovation Horizon 2020 (Grant
669 Agreement 674899). The authors thank M. Rudolf, F. Neumann, and Th. Ziegenhagen for their
670 helpful discussion and assistance during our laboratory experiments. Some uniform colormaps
671 are adapted from Cramer, (2018).

672

References

- 674 Adam, J., Urai, J. L., Wieneke, B., Oncken, O., Pfeiffer, K., Kukowski, N., Lohrmann, J., Hoth,
675 S., Van Der Zee, W., & Schmatz, J. (2005). Shear localisation and strain distribution during
676 tectonic faulting—New insights from granular-flow experiments and high-resolution optical
677 image correlation techniques. *Journal of Structural Geology*, 27(2), 283–301.
- 678 Atwater, B. F., Furukawa, R., Hemphill-Haley, E., Ikeda, Y., Kashima, K., Kawase, K., Kelsey,
679 H. M., Moore, A. L., Nanayama, F., Nishimura, Y., Odagiri, S., Ota, Y., Park, S.-C., Satake,
680 K., Sawai, Y., & Shimokawa, K. (2016). Seventeenth-century uplift in eastern Hokkaido,
681 Japan: [Http://Dx.Doi.Org/10.1191/0959683604hl726rp](http://dx.doi.org/10.1191/0959683604hl726rp), 14(4), 487–501.
682 <https://doi.org/10.1191/0959683604HL726RP>
- 683 Baker, A., Allmendinger, R. W., Owen, L. A., & Rech, J. A. (2013). Permanent deformation
684 caused by subduction earthquakes in northern Chile. *Nature Geoscience* 2013 6:6, 6(6),
685 492–496. <https://doi.org/10.1038/ngeo1789>
- 686 Caniven, Y., & Dominguez, S. (2021). Validation of a Multilayered Analog Model Integrating
687 Crust-Mantle Visco-Elastic Coupling to Investigate Subduction Megathrust Earthquake
688 Cycle. *Journal of Geophysical Research: Solid Earth*, 126(2), e2020JB020342.
689 <https://doi.org/10.1029/2020JB020342>

- 690 Chlieh, M., Avouac, J. P., Sieh, K., Natawidjaja, D. H., & Galetzka, J. (2008). Heterogeneous
691 coupling of the Sumatran megathrust constrained by geodetic and paleogeodetic
692 measurements. *Journal of Geophysical Research: Solid Earth*, *113*, 5305.
693 <https://doi.org/10.1029/2007JB004981>
- 694 Chlieh, M., De Chabalier, J. B., Ruegg, J. C., Armijo, R., Dmowska, R., Campos, J., & Feigl, K.
695 L. (2004). Crustal deformation and fault slip during the seismic cycle in the North Chile
696 subduction zone, from GPS and InSAR observations. *Geophysical Journal International*,
697 *158*(2), 695–711. <https://doi.org/10.1111/J.1365-246X.2004.02326.X>
- 698 Clark, K., Howarth, J., Litchfield, N., Cochran, U., Turnbull, J., Dowling, L., Howell, A.,
699 Berryman, K., & Wolfe, F. (2019). Geological evidence for past large earthquakes and
700 tsunamis along the Hikurangi subduction margin, New Zealand. *Marine Geology*, *412*, 139–
701 172. <https://doi.org/10.1016/J.MARGEO.2019.03.004>
- 702 Collot, J.-Y., Agudelo, W., Ribodetti, A., & Marcaillou, B. (2008). Origin of a crustal splay fault
703 and its relation to the seismogenic zone and underplating at the erosional north Ecuador–
704 south Colombia oceanic margin. *Journal of Geophysical Research: Solid Earth*, *113*(B12),
705 12102. <https://doi.org/10.1029/2008JB005691>
- 706 Collot, Jean-Yves, Marcaillou, B., Sage, F., Michaud, F., Agudelo, W., Charvis, P., Graindorge,
707 D., Gutscher, M.-A., & Spence, G. (2004). Are rupture zone limits of great subduction
708 earthquakes controlled by upper plate structures? Evidence from multichannel seismic
709 reflection data acquired across the northern Ecuador–southwest Colombia margin. *Journal*
710 *of Geophysical Research: Solid Earth*, *109*(B11), 1–14.
711 <https://doi.org/10.1029/2004JB003060>
- 712 Corbi, F., Sandri, L., Bedford, J., Funicello, F., Brizzi, S., Rosenau, M., & Lallemand, S. (2019).
713 Machine Learning Can Predict the Timing and Size of Analog Earthquakes. *Geophysical*
714 *Research Letters*, *46*(3), 1303–1311. <https://doi.org/10.1029/2018GL081251>
- 715 Corbi, Fabio, Bedford, J., Sandri, L., Funicello, F., Gualandi, A., & Rosenau, M. (2020).
716 Predicting imminence of analog megathrust earthquakes with Machine Learning:
717 Implications for monitoring subduction zones. *Geophysical Research Letters*, *47*(7),
718 e2019GL086615. <https://doi.org/10.1029/2019GL086615>

- 719 Corbi, Fabio, Herrendörfer, R., Funicello, F., & van Dinther, Y. (2017). Controls of seismogenic
720 zone width and subduction velocity on interplate seismicity: Insights from analog and
721 numerical models. *Geophysical Research Letters*, *44*(12), 6082–6091.
722 <https://doi.org/10.1002/2016GL072415>
- 723 Cramer, F. (2018). *Scientific colour-maps*. <https://doi.org/10.5281/ZENODO.1287763>
- 724 Cubas, N., Avouac, J. P., Leroy, Y. M., & Pons, A. (2013a). Low friction along the high slip
725 patch of the 2011 Mw 9.0 Tohoku-Oki earthquake required from the wedge structure and
726 extensional splay faults. *Geophysical Research Letters*, *40*(16), 4231–4237.
727 <https://doi.org/10.1002/grl.50682>
- 728 Cubas, Nadaya, Avouac, J. P., Souloumiac, P., & Leroy, Y. (2013b). Megathrust friction
729 determined from mechanical analysis of the forearc in the Maule earthquake area. *Earth and*
730 *Planetary Science Letters*, *381*, 92–103. <https://doi.org/10.1016/j.epsl.2013.07.037>
- 731 Cubas, Nadaya, Souloumiac, P., & Singh, S. C. (2016). Relationship link between landward
732 vergence in accretionary prisms and tsunami generation. *GEOLOGY*, *44*.
733 <https://doi.org/10.1130/G38019.1>
- 734 Dahlen, F. A., Suppe, J., & Davis, D. (1984). Mechanics of fold-and-thrust belts and accretionary
735 wedges: Cohesive Coulomb Theory. *Journal of Geophysical Research: Solid Earth*,
736 *89*(B12), 10087–10101. <https://doi.org/10.1029/JB089IB12P10087>
- 737 Delano, J. E., Amos, C. B., Loveless, J. P., Rittenour, T. M., Sherrod, B. L., & Lynch, E. M.
738 (2017). Influence of the megathrust earthquake cycle on upper-plate deformation in the
739 Cascadia forearc of Washington State, USA. *Geology*, *45*(11), 1051–1054.
740 <https://doi.org/10.1130/G39070.1>
- 741 Encinas, A., Finger, K. L., Buatois, L. A., & Peterson, D. E. (2012). Major forearc subsidence
742 and deep-marine Miocene sedimentation in the present Coastal Cordillera and Longitudinal
743 Depression of south-central Chile (38°30'S–41°45'S). *GSA Bulletin*, *124*(7–8), 1262–1277.
744 <https://doi.org/10.1130/B30567.1>
- 745 Farías, M., Comte, D., Roecker, S., Carrizo, D., & Pardo, M. (2011). Crustal extensional faulting
746 triggered by the 2010 Chilean earthquake: The Pichilemu Seismic Sequence. *Tectonics*,

- 747 30(6). <https://doi.org/10.1029/2011TC002888>
- 748 Fuller, C. W., Willett, S. D., & Brandon, M. T. (2006). Formation of forearc basins and their
749 influence on subduction zone earthquakes. *Geology*, *34*(2), 65–68.
750 <https://doi.org/10.1130/G21828.1>
- 751 Geersen, J., Ranero, C. R., Kopp, H., Behrmann, J. H., Lange, D., Klaucke, I., Barrientos, S.,
752 Diaz-Naveas, J., Barckhausen, U., & Reichert, C. (2018). Does permanent extensional
753 deformation in lower forearc slopes indicate shallow plate-boundary rupture? *Earth and*
754 *Planetary Science Letters*, *489*, 17–27. <https://doi.org/10.1016/j.epsl.2018.02.030>
- 755 Geersen, J., Scholz, F., Linke, P., Schmidt, M., Lange, D., Behrmann, J. H., Völker, D., &
756 Hensen, C. (2016). Fault zone controlled seafloor methane seepage in the rupture area of the
757 2010 Maule earthquake, Central Chile. *Geochemistry, Geophysics, Geosystems*, *17*(11),
758 4802–4813. <https://doi.org/10.1002/2016GC006498>
- 759 González-Alfaro, J., Vargas, G., Ortlieb, L., González, G., Ruiz, S., Báez, J. C., Mandeng-Yogo,
760 M., Caquineau, S., Álvarez, G., del Campo, F., & del Río, I. (2018). Abrupt increase in the
761 coastal uplift and earthquake rate since ~40 ka at the northern Chile seismic gap in the
762 Central Andes. *Earth and Planetary Science Letters*, *502*, 32–45.
763 <https://doi.org/10.1016/J.EPSL.2018.08.043>
- 764 Herman, M. W., & Govers, R. (2020). Stress evolution during the megathrust earthquake cycle
765 and its role in triggering extensional deformation in subduction zones. *Earth and Planetary*
766 *Science Letters*, *544*, 116379. <https://doi.org/10.1016/J.EPSL.2020.116379>
- 767 Hu, Y., & Wang, K. (2008). Coseismic strengthening of the shallow portion of the subduction
768 fault and its effects on wedge taper. *Journal of Geophysical Research: Solid Earth*,
769 *113*(B12), 12411. <https://doi.org/10.1029/2008JB005724>
- 770 Ito, Y., Tsuji, T., Osada, Y., Kido, M., Inazu, D., Hayashi, Y., Tsushima, H., Hino, R., &
771 Fujimoto, H. (2011). Frontal wedge deformation near the source region of the 2011
772 Tohoku-Oki earthquake. *Geophysical Research Letters*, *38*(7).
773 <https://doi.org/10.1029/2011GL048355>
- 774 Jara-Muñoz, J., Melnick, D., Brill, D., & Strecker, M. R. (2015). Segmentation of the 2010

- 775 Maule Chile earthquake rupture from a joint analysis of uplifted marine terraces and
776 seismic-cycle deformation patterns. *Quaternary Science Reviews*, 113(1), 171–192.
777 <https://doi.org/10.1016/J.QUASCIREV.2015.01.005>
- 778 King Hubbert, M. (1937). Theory of scale models as applied to the study of geologic structures.
779 *Bulletin of the Geological Society of America*, 48(10), 1459–1520.
780 <https://doi.org/10.1130/GSAB-48-1459>
- 781 Kopp, H. (2013). Invited review paper: The control of subduction zone structural complexity and
782 geometry on margin segmentation and seismicity. *Tectonophysics*, 589, 1–16.
783 <https://doi.org/10.1016/J.TECTO.2012.12.037>
- 784 Kosari, E., Rosenau, M., Bedford, J., Rudolf, M., & Oncken, O. (2020). On the Relationship
785 Between Offshore Geodetic Coverage and Slip Model Uncertainty: Analog Megathrust
786 Earthquake Case Studies. *Geophysical Research Letters*, 47(15).
787 <https://doi.org/10.1029/2020GL088266>
- 788 Kuehn, N. M., Hainzl, S., & Scherbaum, F. (2008). Non-Poissonian earthquake occurrence in
789 coupled stress release models and its effect on seismic hazard. *Geophysical Journal*
790 *International*, 174(2), 649–658. <https://doi.org/10.1111/J.1365-246X.2008.03835.X>
- 791 Lay, T., Kanamori, H., Ammon, C. J., Koper, K. D., Hutko, A. R., Ye, L., Yue, H., & Rushing,
792 T. M. (2012). Depth-varying rupture properties of subduction zone megathrust faults.
793 *Journal of Geophysical Research: Solid Earth*, 117(4).
794 <https://doi.org/10.1029/2011JB009133>
- 795 Lieser, K., Grevemeyer, I., Lange, D., Flueh, E., Tilmann, F., & Contreras-Reyes, E. (2014).
796 Splay fault activity revealed by aftershocks of the 2010 Mw 8.8 Maule earthquake, central
797 Chile. *Geology*, 42(9), 823–826. <https://doi.org/10.1130/G35848.1>
- 798 Loveless, J. P., Allmendinger, R. W., Pritchard, M. E., Garroway, J. L., & González, G. (2009).
799 Surface cracks record long-term seismic segmentation of the Andean margin. *Geology*,
800 37(1), 23–26. <https://doi.org/10.1130/G25170A.1>
- 801 Loveless, J. P., Allmendinger, R. W., Pritchard, M. E., & González, G. (2010). Normal and
802 reverse faulting driven by the subduction zone earthquake cycle in the northern Chilean fore

- 803 arc. *Tectonics*, 29(2). <https://doi.org/10.1029/2009TC002465>
- 804 Loveless, J. P., Hoke, G. D., Allmendinger, R. W., González, G., Isacks, B. L., & Carrizo, D. A.
805 (2005). Pervasive cracking of the northern Chilean Coastal Cordillera: New evidence for
806 forearc extension. *Geology*, 33(12), 973–976. <https://doi.org/10.1130/G22004.1>
- 807 Loveless, J. P., & Meade, B. J. (2011). Spatial correlation of interseismic coupling and coseismic
808 rupture extent of the 2011 MW= 9.0 Tohoku-oki earthquake. *Geophysical Research Letters*,
809 38(17). <https://doi.org/10.1029/2011GL048561>
- 810 Madella, A., & Ehlers, T. A. (2021). Contribution of background seismicity to forearc uplift.
811 *Nature Geoscience* 2021, 1–6. <https://doi.org/10.1038/s41561-021-00779-0>
- 812 Maksymowicz, A., Ruiz, J., Vera, E., Contreras-Reyes, E., Ruiz, S., Arraigada, C., Bonvalot, S.,
813 & Bascuñan, S. (2018). Heterogeneous structure of the Northern Chile marine forearc and
814 its implications for megathrust earthquakes. *Geophysical Journal International*, 215(2),
815 1080–1097. <https://doi.org/10.1093/gji/ggy325>
- 816 Malatesta, L. C., Bruhat, L., Finnegan, N. J., & Olive, J.-A. L. (2021). Co-location of the
817 Dwindip End of Seismic Coupling and the Continental Shelf Break. *Journal of*
818 *Geophysical Research: Solid Earth*, 126(1), e2020JB019589.
819 <https://doi.org/10.1029/2020JB019589>
- 820 Matsu'ura, T., Komatsubara, J., & Wu, C. (2019). Accurate determination of the Pleistocene
821 uplift rate of the NE Japan forearc from the buried MIS 5e marine terrace shoreline angle.
822 *Quaternary Science Reviews*, 212, 45–68.
823 <https://doi.org/10.1016/J.QUASCIREV.2019.03.007>
- 824 McCaffrey, R., King, R. W., Payne, S. J., & Lancaster, M. (2013). Active tectonics of
825 northwestern U.S. inferred from GPS-derived surface velocities. *Journal of Geophysical*
826 *Research: Solid Earth*, 118(2), 709–723. <https://doi.org/10.1029/2012JB009473>
- 827 Melnick, D., Bookhagen, B., Strecker, M. R., & Echtler, H. P. (2009). Segmentation of
828 megathrust rupture zones from fore-arc deformation patterns over hundreds to millions of
829 years, Arauco peninsula, Chile. *Journal of Geophysical Research: Solid Earth*, 114(B1),
830 1407. <https://doi.org/10.1029/2008JB005788>

- 831 Melnick, D., Li, S., Moreno, M., Cisternas, M., Jara-Muñoz, J., Wesson, R., Nelson, A., Báez, J.
832 C., & Deng, Z. (2018). Back to full interseismic plate locking decades after the giant 1960
833 Chile earthquake. *Nature Communications* 2018 9:1, 9(1), 1–10.
834 <https://doi.org/10.1038/s41467-018-05989-6>
- 835 Menant, A., Angiboust, S., Gerya, T., Lacassin, R., Simoes, M., & Grandin, R. (2020). Transient
836 stripping of subducting slabs controls periodic forearc uplift. *Nature Communications* 2020
837 11:1, 11(1), 1–10. <https://doi.org/10.1038/s41467-020-15580-7>
- 838 Métois, M., Socquet, A., Vigny, C., Carrizo, D., Peyrat, S., Delorme, A., Maureira, E., Valderas-
839 Bermejo, M.-C., & Ortega, I. (2013). Revisiting the North Chile seismic gap segmentation
840 using GPS-derived interseismic coupling. *Geophysical Journal International*, 194(3), 1283–
841 1294. <https://doi.org/10.1093/GJI/GGT183>
- 842 Molina, D., Tassara, A., Abarca, R., Melnick, D., & Madella, A. (2021). Frictional Segmentation
843 of the Chilean Megathrust From a Multivariate Analysis of Geophysical, Geological, and
844 Geodetic Data. *Journal of Geophysical Research: Solid Earth*, 126(6), e2020JB020647.
845 <https://doi.org/10.1029/2020JB020647>
- 846 Moreno, M., Rosenau, M., & Oncken, O. (2010). 2010 Maule earthquake slip correlates with
847 pre-seismic locking of Andean subduction zone. *Nature* 2010 467:7312, 467(7312), 198–
848 202. <https://doi.org/10.1038/nature09349>
- 849 Moreno, M. S., Bolte, J., Klotz, J., & Melnick, D. (2009). Impact of megathrust geometry on
850 inversion of coseismic slip from geodetic data: Application to the 1960 Chile earthquake.
851 *Geophysical Research Letters*, 36(16), 16310. <https://doi.org/10.1029/2009GL039276>
- 852 Moscoso, E., Grevemeyer, I., Contreras-Reyes, E., Flueh, E. R., Dzierma, Y., Rabbal, W., &
853 Thorwart, M. (2011). Revealing the deep structure and rupture plane of the 2010 Maule,
854 Chile earthquake (Mw = 8.8) using wide angle seismic data. *Earth and Planetary Science*
855 *Letters*, 307(1–2), 147–155. <https://doi.org/10.1016/J.EPSL.2011.04.025>
- 856 Mouslopoulou, V., Oncken, O., Hainzl, S., & Nicol, A. (2016). Uplift rate transients at
857 subduction margins due to earthquake clustering. *Tectonics*, 35(10), 2370–2384.
858 <https://doi.org/10.1002/2016TC004248>

- 859 Niwa, Y., Sugai, T., Matsushima, Y., & Toda, S. (2017). Subsidence along the central to
860 southern Sanriku coast, northeast Japan, near the source region of the 2011 Tohoku-oki
861 earthquake, estimated from the Holocene sedimentary succession along a ria coast.
862 *Quaternary International*, 456, 1–16. <https://doi.org/10.1016/J.QUAINT.2017.08.008>
- 863 Noda, H., & Lapusta, N. (2013). Stable creeping fault segments can become destructive as a
864 result of dynamic weakening. *Nature* 2013 493:7433, 493(7433), 518–521.
865 <https://doi.org/10.1038/nature11703>
- 866 Normand, R., Simpson, G., Herman, F., Haque Biswas, R., Bahroudi, A., & Schneider, B.
867 (2019). Dating and morpho-stratigraphy of uplifted marine terraces in the Makran
868 subduction zone (Iran). *Earth Surface Dynamics*, 7(1), 321–344.
869 <https://doi.org/10.5194/ESURF-7-321-2019>
- 870 Oleskevich, D. A., Hyndman, R. D., & Wang, K. (1999). The updip and downdip limits to great
871 subduction earthquakes: Thermal and structural models of Cascadia, south Alaska, SW
872 Japan, and Chile. *Journal of Geophysical Research: Solid Earth*, 104(B7), 14965–14991.
873 <https://doi.org/10.1029/1999JB900060>
- 874 Ott, R. F., Gallen, S. F., Wegmann, K. W., Biswas, R. H., Herman, F., & Willett, S. D. (2019).
875 Pleistocene terrace formation, Quaternary rock uplift rates and geodynamics of the Hellenic
876 Subduction Zone revealed from dating of paleoshorelines on Crete, Greece. *Earth and
877 Planetary Science Letters*, 525, 115757. <https://doi.org/10.1016/J.EPSL.2019.115757>
- 878 Ozawa, S., Nishimura, T., Suito, H., Kobayashi, T., Tobita, M., & Imakiire, T. (2011). Coseismic
879 and postseismic slip of the 2011 magnitude-9 Tohoku-Oki earthquake. *Nature*, 475(7356),
880 373–377. <https://doi.org/10.1038/nature10227>
- 881 Pastén-Araya, F., Potin, B., Ruiz, S., Zerbst, L., Aden-Antoniów, F., Azúa, K., Rivera, E.,
882 Rietbrock, A., Salazar, P., & Fuenzalida, A. (2021). Seismicity in the upper plate of the
883 Northern Chilean offshore forearc: Evidence of splay fault south of the Mejillones
884 Peninsula. *Tectonophysics*, 800, 228706. <https://doi.org/10.1016/j.tecto.2020.228706>
- 885 Pritchard, M. E., Simons, M., Rosen, P. A., Hensley, S., & Webb, F. H. (2002). Co-seismic slip
886 from the 1995 July 30 Mw= 8.1 Antofagasta, Chile, earthquake as constrained by InSAR

- 887 and GPS observations. *Geophysical Journal International*, 150(2), 362–376.
888 <https://doi.org/10.1046/J.1365-246X.2002.01661.X>
- 889 Reginato, G., Vera, E., Contreras-Reyes, E., Tréhu, A. M., Maksymowicz, A., Bello-González, J.
890 P., & González, F. (2020). Seismic structure and tectonics of the continental wedge
891 overlying the source region of the Iquique Mw8.1 2014 earthquake. *Tectonophysics*, 796,
892 228629. <https://doi.org/10.1016/j.tecto.2020.228629>
- 893 Reid, H. F. (1910). The mechanism of the earthquake, the california earthquake of April 18,
894 1906, Report of the state earthquake investigation commission. In *Washington DC:*
895 *Carnegie Institution* (Vol. 2).
- 896 Rosenau, M., Corbi, F., & Dominguez, S. (2017). Analogue earthquakes and seismic cycles:
897 Experimental modelling across timescales. *Solid Earth*, 8(3), 597–635.
898 <https://doi.org/10.5194/SE-8-597-2017>
- 899 Rosenau, M., Horenko, I., Corbi, F., Rudolf, M., Kornhuber, R., & Oncken, O. (2019).
900 Synchronization of Great Subduction Megathrust Earthquakes: Insights From Scale Model
901 Analysis. *Journal of Geophysical Research: Solid Earth*, 124(4), 3646–3661.
902 <https://doi.org/10.1029/2018JB016597>
- 903 Rosenau, M., Lohrmann, J., & Oncken, O. (2009). Shocks in a box: An analogue model of
904 subduction earthquake cycles with application to seismotectonic forearc evolution. *Journal*
905 *of Geophysical Research: Solid Earth*, 114(B1), 1409.
906 <https://doi.org/10.1029/2008JB005665>
- 907 Rosenau, M., Nerlich, R., Brune, S., & Oncken, O. (2010). Experimental insights into the scaling
908 and variability of local tsunamis triggered by giant subduction megathrust earthquakes.
909 *Journal of Geophysical Research: Solid Earth*, 115(9).
910 <https://doi.org/10.1029/2009JB007100>
- 911 Rosenau, M., & Oncken, O. (2009). Fore-arc deformation controls frequency-size distribution of
912 megathrust earthquakes in subduction zones. *Journal of Geophysical Research*, 114(B10),
913 B10311. <https://doi.org/10.1029/2009JB006359>
- 914 Ruff, L. J., & Tichelaar, B. W. (1996). What Controls the Seismogenic Plate Interface in

- 915 Subduction Zones? *Geophysical Monograph Series*, 96, 105–111.
916 <https://doi.org/10.1029/GM096P0105>
- 917 Ruh, J. B. (2020). Numerical modeling of tectonic underplating in accretionary wedge systems.
918 *Geosphere*, 16(6), 1385–1407. <https://doi.org/10.1130/GES02273.1>
- 919 Saillard, M., Audin, L., Rousset, B., Avouac, J.-P., Chlieh, M., Hall, S. R., Husson, L., & Farber,
920 D. L. (2017). From the seismic cycle to long-term deformation: linking seismic coupling
921 and Quaternary coastal geomorphology along the Andean megathrust. *Tectonics*, 36(2),
922 241–256. <https://doi.org/10.1002/2016TC004156>
- 923 Sawai, Y. (2020). Subduction zone paleoseismology along the Pacific coast of northeast Japan
924 — progress and remaining problems. *Earth-Science Reviews*, 208, 103261.
925 <https://doi.org/10.1016/J.EARSCIREV.2020.103261>
- 926 Sawai, Y., Satake, K., Kamataki, T., Nasu, H., Shishikura, M., Atwater, B. F., Horton, B. P.,
927 Kelsey, H. M., Nagumo, T., & Yamaguchi, M. (2004). Transient Uplift After a 17th-
928 Century Earthquake Along the Kuril Subduction Zone. *Science*, 306(5703), 1918–1920.
929 <https://doi.org/10.1126/SCIENCE.1104895>
- 930 Schmalzle, G. M., McCaffrey, R., & Creager, K. C. (2014). Central Cascadia subduction zone
931 creep. *Geochemistry, Geophysics, Geosystems*, 15(4), 1515–1532.
932 <https://doi.org/10.1002/2013GC005172>
- 933 Schurr, B., Moreno, M., Tréhu, A. M., Bedford, J., Kummerow, J., Li, S., & Oncken, O. (2020).
934 Forming a Mogi Doughnut in the Years Prior to and Immediately Before the 2014 M8.1
935 Iquique, Northern Chile, Earthquake. *Geophysical Research Letters*, 47(16),
936 e2020GL088351. <https://doi.org/10.1029/2020GL088351>
- 937 Shennan, I., & Hamilton, S. (2006). Coseismic and pre-seismic subsidence associated with great
938 earthquakes in Alaska. *Quaternary Science Reviews*, 25(1–2), 1–8.
939 <https://doi.org/10.1016/J.QUASCIREV.2005.09.002>
- 940 Simons, M., Minson, S. E., Sladen, A., Ortega, F., Jiang, J., Owen, S. E., Meng, L., Ampuero, J.-
941 P., Wei, S., Chu, R., Helmberger, D. V., Kanamori, H., Hetland, E., Moore, A. W., &
942 Webb, F. H. (2011). The 2011 Magnitude 9.0 Tohoku-Oki Earthquake: Mosaicking the

- 943 Megathrust from Seconds to Centuries. *Science*, 332(6036), 1421–1425.
944 <https://doi.org/10.1126/SCIENCE.1206731>
- 945 Song, T. R. A., & Simons, M. (2003). Large trench-parallel gravity variations predict
946 seismogenic behavior in subduction zones. *Science*, 301(5633), 630–633.
947 <https://doi.org/10.1126/science.1085557>
- 948 Soto, H., Sippl, C., Schurr, B., Kummerow, J., Asch, G., Tilmann, F., Comte, D., Ruiz, S., &
949 Oncken, O. (2019). Probing the Northern Chile Megathrust With Seismicity: The 2014
950 M8.1 Iquique Earthquake Sequence. *Journal of Geophysical Research: Solid Earth*,
951 124(12), 12935–12954. <https://doi.org/10.1029/2019JB017794>
- 952 Storch, I., Buske, S., Victor, P., & Oncken, O. (2021). Seismic images of the Northern Chilean
953 subduction zone at 19°40'S, prior to the 2014 Iquique earthquake. *Geophysical Journal
954 International*, 225(2), 1048–1061. <https://doi.org/10.1093/gji/ggab035>
- 955 Sun, T., Wang, K., Fujiwara, T., Kodaira, S., & He, J. (2017). Large fault slip peaking at trench
956 in the 2011 Tohoku-oki earthquake. *Nature Communications*, 8(1), 1–8.
957 <https://doi.org/10.1038/ncomms14044>
- 958 Tilmann, F., Zhang, Y., Moreno, M., Saul, J., Eckelmann, F., Palo, M., Deng, Z., Babeyko, A.,
959 Chen, K., Baez, J. C., Schurr, B., Wang, R., & Dahm, T. (2016). The 2015 Illapel
960 earthquake, central Chile: A type case for a characteristic earthquake? *Geophysical
961 Research Letters*, 43(2), 574–583. <https://doi.org/10.1002/2015GL066963>
- 962 Tsuji, T., Ito, Y., Kido, M., Osada, Y., Fujimoto, H., Ashi, J., Kinoshita, M., & Matsuoka, T.
963 (2011). Potential tsunamigenic faults of the 2011 off the Pacific coast of Tohoku
964 Earthquake. *Earth, Planets and Space 2011 63:7*, 63(7), 831–834.
965 <https://doi.org/10.5047/EPS.2011.05.028>
- 966 Tsuji, T., Kawamura, K., Kanamatsu, T., Kasaya, T., Fujikura, K., Ito, Y., Tsuru, T., &
967 Kinoshita, M. (2013). Extension of continental crust by anelastic deformation during the
968 2011 Tohoku-oki earthquake: The role of extensional faulting in the generation of a great
969 tsunami. *Earth and Planetary Science Letters*, 364, 44–58.
970 <https://doi.org/10.1016/j.epsl.2012.12.038>

- 971 Wallace, L. M., Barnes, P., Beavan, J., Dissen, R. Van, Litchfield, N., Mountjoy, J., Langridge,
972 R., Lamarche, G., & Pondard, N. (2012). The kinematics of a transition from subduction to
973 strike-slip: An example from the central New Zealand plate boundary. *Journal of*
974 *Geophysical Research: Solid Earth*, 117(B2), 2405. <https://doi.org/10.1029/2011JB008640>
- 975 Wang, K., Brown, L., Hu, Y., Yoshida, K., He, J., & Sun, T. (2019). Stable Forearc Stressed by a
976 Weak Megathrust: Mechanical and Geodynamic Implications of Stress Changes Caused by
977 the M = 9 Tohoku-Oki Earthquake. *Journal of Geophysical Research: Solid Earth*, 124(6),
978 6179–6194. <https://doi.org/10.1029/2018JB017043>
- 979 Wang, K., & Hu, Y. (2006). Accretionary prisms in subduction earthquake cycles: The theory of
980 dynamic Coulomb wedge. *Journal of Geophysical Research: Solid Earth*, 111(6), 6410.
981 <https://doi.org/10.1029/2005JB004094>
- 982 Wang, K., & Tréhu, A. M. (2016). Invited review paper: Some outstanding issues in the study of
983 great megathrust earthquakes—The Cascadia example. In *Journal of Geodynamics* (Vol.
984 98, pp. 1–18). Elsevier Ltd. <https://doi.org/10.1016/j.jog.2016.03.010>
- 985 Wells, R. E., Blakely, R. J., Sugiyama, Y., Scholl, D. W., & Dinterman, P. A. (2003). Basin-
986 centered asperities in great subduction zone earthquakes: A link between slip, subsidence,
987 and subduction erosion? *Journal of Geophysical Research: Solid Earth*, 108(B10), 2507.
988 <https://doi.org/10.1029/2002jb002072>
- 989 Williamson, A. L., & Newman, A. V. (2018). Limitations of the Resolvability of Finite-Fault
990 Models Using Static Land-Based Geodesy and Open-Ocean Tsunami Waveforms. *Journal*
991 *of Geophysical Research: Solid Earth*, 123(10), 9033–9048.
992 <https://doi.org/10.1029/2018JB016091>